Supporting Information

Synergy of rare earth single atoms and Pt nanoclusters@N-doped carbon for improved alkaline hydrogen evolution

Peng Wang,[a] Ping Bai,[a] Xiao Han,[a] Jiarong Mu,[a] Min Li,[a] Yihua Zhao,[a] Jing Xu,[a] Xudong Liu,[a] Zhinan Xie,[a] Yilin Wang,[b] Fenghua Bai,*[a] Jinlu He,*[a] Yiguo Su,*[a] and Ling Huang*[b]

Experimental Section

Synthesis of Pr_{SAs}@NDC

First, zinc acetate (4 mmol, 99%, Macklin) and $Pr(NO_3)_3 \cdot 6H_2O$ (0.1 mmol, 99%, Macklin) were dissolved in 80 mL of ultrapure water (>18 MΩ·cm), which was named solution A. Dissolve 2-methylimidazole (48 mmol, 98%, Macklin) in 80 mL of ultrapure water and designate the resulting solution as B. Slowly drip solution B into solution A, then stir the mixture at room temperature for 6 h. The solution was centrifuged with ultrapure water and ethanol, and the resulting white precipitate was dried at 60 ℃. The resulting white powder was heated in a tube furnace to 900 °C at a heating rate of 5 °C·min^{-1} for 3 h in an Ar atmosphere. Then, the black powder was soaked in 1 M HCl for 6 h, washed with ultrapure water several times, and finally dried at 60 ℃. The preparation of NDC was similar to that of Pr_{SAs}@NDC, except that $Pr(NO_3)_3 \cdot 6H_2O$ was not included. The preparation method for Ce_{SAs}@NDC, Gd_{SAs}@NDC, and Sm_{SAs}@NDC is identical to that of Pr_{SAs}@NDC, with the only difference being the substitution of $Pr(NO_3)_3 \cdot 6H_2O$ (99%, Macklin) with $Ce(NO_3)_3 \cdot 6H_2O$ (99%, Macklin), $Gd(NO_3)_3 \cdot 6H_2O$ (99%, Macklin), and $Sm(NO_3)_3 \cdot 6H_2O$ (99%, Macklin), respectively.

The formation of 2D-like structure is attributed to the stacking effect of Ce^{3+} with 2-methylimidazole and the coordination effect of carboxylate during self-assembly.[1] Ce^{3+} has a larger ionic radius and higher coordination number than Zn^{2+}, causing it to compete with Zn^{2+} for coordination sites on 2-methylimidazole. Since the formation of a well-ordered ZIF-8 framework relies on precise bond angles and spatial arrangements between Zn^{2+} and imidazole ligands, introduction of Ce^{3+}disrupts this regularity locally and hinders uniform three-dimensional crystal growth. Moreover, carboxylate ions can selectively passivate the Zn sites on the surface, further inhibiting the growth in the direction perpendicular to the layers, thereby stabilizing and promoting the formation of a 2D-like structure.[2]

Synthesis of Pt_{NCs}-Pr_{SAs}@NDC

Triphenylphosphine (PPh_3)-coordinated Pt_6 cluster was prepared according to a reported method.[3] Typically, 200 μL of toluene containing PPh_3 (50 mM, 99%, Macklin), 100 μL of an aqueous solution of $H_2PtCl_6 \cdot 6H_2O$ (50 mM, 37.5%, Macklin), and 4.5 mL of ethanol was stirred for 2 h. After that, 100 μL of ethanol containing a borane-tertbutylamine complex (TBAB, 100 mM, ≥95.0%) was added into the above solution under stirring. The solution was allowed to react for 2 h. Unlike the strong reducing agent $NaBH_4$, TBAB exhibits a mild and controlled reducing property with a moderate reduction potential (≈ -0.8 V vs. SHE) (Fig. S44).[4] To prepare Pt_{NCs}-Pr_{SAs}@NDC, Pr_{SAs}@NDC (20 mg) was first ultrasonically dispersed in 45 mL of ethanol. Then, the above PPh_3-coordinated Pt_6 cluster suspension was dropwise added into the solution and stirred for 6 h. The sample was collected via vacuum filtration, washed with ethanol, and vacuum dried at 60 ℃ for 6 h. The preparation method for Pt_{NCs}-Gd_{SAs}@NDC and Pt_{NCs}-Sm_{SAs}@NDC is identical to that of Pt_{NCs}-Pr_{SAs}@NDC, with the only difference being the substitution of Pr_{SAs}@NDC with Gd_{SAs}@NDC and Sm_{SAs}@NDC.

Synthesis of NiFe layered double hydroxide (NiFe-LDH)

Firstly, the solution was prepared simply by dissolving 0.5 mmol $Ni(NO_3)_2 \cdot 6H_2O$, 0.5 mmol $Fe(NO_3)_3 \cdot 9H_2O$, and 5 mmol $(NH_2)_2CO$ in 35 mL DI water. Then, the solution with a piece of NF (1×2 cm) was transferred into a 50 mL Teflon-lined autoclave and kept at 120 °C for 12 h. The obtained self-supporting electrodes were washed several times with deionized water followed by vacuum drying for 12 h.[5]

Characterization

XRD was conducted using a PuXi XD3 diffractometer equipped with Cu Kα radiation and featuring a graphite monochromator (k = 0.15406 nm). XPS analysis was conducted using Thermo ESCALAB 250 to examine the surface electronic states and chemical composition of the samples. TEM images were collected using a Hitachi H-800 TEM. AC HAADF-STEM was used to observe metal dispersion at the atomic scale. EDS was used to observe dispersion of

elements. A JEOL 200F TEM equipped with a probe spherical aberration corrector was used to take HAADF-STEM and EDS images at 200 keV. ICP-OES was used to detect metal loading in catalysts. XAS spectra was performed with Si (311) crystal monochromators at the BL11B beamlines at the Shanghai Synchrotron Radiation Facility (SSRF) (Shanghai, China). The spectra were processed and analyzed by the software codes Athena and Artemis.

Electrochemical measurements

Electrochemical measurements were conducted on a CHI 760E Electrochemical Workstation (Shanghai Chenhua Instrument Co., Ltd., China) in a conventional three-electrode cell. A graphite rod and Hg/HgO electrodes were used as the counter electrode and reference electrode, respectively. The working electrode was a glassy carbon electrode (GCE, diameter: 5 mm, area: 0.0196 cm^2). All observed potentials vs. Hg/HgO were calibrated to a reversible hydrogen electrode (RHE) according to the Nernst equation. ($E_{RHE} = E_{Hg/HgO} + 0.0591 \times pH + 0.098$). The working electrode was prepared as follows: 5 mg of catalyst was dispersed in a mixture of ethanol (100 μL) and Nafion (5 wt%, 10 μL) under ultrasonication for 2 h. A certain volume of catalyst ink was dropped onto the GCE surface for further electrochemical tests. The catalyst loading amount was determined as 1.25 $mg \cdot cm^{-2}$. Based on the ICP-OES results, the Pt loading amounts of Pt_{NCs}-Pr_{SAs}@NDC and Pt_{NCs}@NDC are 0.022 $mg_{Pt} \cdot cm^{-2}$ and 0.024 $mg_{Pt} \cdot cm^{-2}$. Besides, the Pt_{NCs}-Pr_{SAs}@NDC was also loaded on the nickel foam to investigate the possibility of Pt_{NCs}-Pr_{SAs}@NDC as electrocatalysts for high-output industrial H_2 production. A 1 × 1 cm^2 catalyst-modified active area was formed by pipetting the catalyst ink onto the nickel foam and drying it at 40 ºC for 0.5 h. The catalyst loading on the nickel foam was 2.5 $mg \cdot cm^{-2}$, with the Pt loading amount being 0.044 $mg_{Pt} \cdot cm^{-2}$. Before performing the LSV experiment, we subjected the CV to electrochemical activation at a scan rate of 50 $mV \cdot s^{-1}$ until the electrode achieved a stable condition. During the LSV tests, we employed a scan rate of 5 $mV \cdot s^{-1}$ with 95% *iR*-compensation. The double-layer capacitance (C_{dl}) of the catalyst was determined at various scanning rates using CV analysis, with measurements conducted in the non-Faraday region. EIS

tests were performed at a given potential in a frequency range of 100 kHz to 0.1 Hz. The stability of the catalysts was tested by means of chronopotentiometry (V-t).

Calculation of TOF

The TOF is calculated by followed Equation (1)-(4):

$$TOF = \frac{N\,H_{2\ per\ unit\ area}}{N_{active\ site\ per\ unit\ area}} \quad (1)$$

$$N\,H_{2\ per\ unit\ area} = \left(|J|\frac{mA}{cm^{-2}}\right)\left(\frac{1Cs^{-1}}{1000\ mA}\right)\left(\frac{1\ mol\ e^{-1}}{96485.3\ C}\right)\left(\frac{1\ mol}{2\ mol\ e^{-1}}\right)\left(\frac{6.022\times10^{23} molecules\ H_2}{1\ mol\ H_2}\right)$$

$$= 3.12\times10^{15}\frac{s^{-1}}{cm^2}|J| \quad (2)$$

$$N_{active\ site\ per\ unit\ area} = N_{Pt\ atom}$$

$$= \left(\frac{catalyst\ loading\ per\ unit\ area\ (x\ g\ cm^{-2})\times Pt\ wt.\%}{Pt\ M_w(g\ mol^{-1})}\right)\left(\frac{6.022\times10^{23} Pt\ atoms}{1\ mol\ Pt}\right) \quad (3)$$

Where J is the measured current density. M_w is the atomic mass of Pt.

For example, the $N_{\text{active site per unit area}}$ for Pt_{NCs}-Pr_{SAs}@NDC was calculated from:

$$N_{active\ site\ per\ unit\ area} = \left(\frac{1.25\times10^{-3} g\ cm^{-2}\times 1.76\ wt.\%}{195.084 g\ mol^{-1}}\right)\left(\frac{6.022\times10^{23}\ Pt\ atoms}{1\ mol\ Pt}\right)$$

$$= 6.804\times10^{16} cm^{-2}$$

Hence, the TOF for Pt_{NCs}-Pr_{SAs}@NDC can be calculated from:

$$TOF = \frac{3.12\times10^{15}\frac{s^{-1}}{cm^2}}{6.804\times10^{16} cm^{-2}}\times|J| = 0.046\times|J| s^{-1} \quad (4)$$

Electrochemical measurements in an AEMWE device

The preparation of slurry: 5 mg of the prepared catalysts and 20 μL of 5 wt.% Poly tetra fluoroethylene (PTFE) dispersion were dispersed in 1.0 mL of isopropanol under sonication treatment and then dried. The mass ratio of the catalyst to PTFE was maintained at 5:1.[6]

A five-layer structure of cathode GDL (porous carbon paper)/catalyst layer/anion exchange membrane/catalyst layer/anode GDL (Ni-foam) integration was adopted. The schematic diagram of AEMWE is presented in Figure S33b. The Pt_{NCs}-Pr_{SAs}@NDC and commercial Pt/C were used as the cathodic catalysts, and homemade NiFe-LDH as the anodic catalyst. The prepared slurries of the cathodic catalysts were first air-sprayed onto porous carbon paper gas diffusion layers (GDLs). The preparation method of homemade NiFe-LDH involves in-situ growth on Ni-foam through a hydrothermal process.[5] Subsequently, the catalyst-coated GDLs were sandwiched with an anion exchange membrane (X3750, Dioxide Materials Sustainion®) to assemble a homemade integrated AEMWE device. The anion exchange membrane was immersed in 1.0 M KOH solution for at least 24 h before used to exchange Cl^- into OH^-. The AEMWE test was conducted at 25, 60, and 80 °C, respectively, with a peristaltic pump delivering 1.0 M KOH at a flow rate of 30 $mL \cdot min^{-1}$.The performance of the AEMWEs was evaluated by measuring the polarization curves from 1.2 to 2.2 V. The stability of the AEMWEs was assessed by measuring the chronopotentiometry at a current density of 500 $mA \cdot cm^{-2}$ and a temperature of 80 ℃. As shown in Figure S33, the dimensions of the electrode working area is 1×1 cm^2. The overall dimensions of the AEMWE device are 6×6×4 cm^3 (length×width×height).

In the majority of the references,[5,7] homemade NiFe LDH is typically employed as the anode catalyst, primarily due to the following two reasons: (1) Among alkaline OER catalysts, NiFe-based materials (particularly those with LDH structures) are widely recognized as one of the most promising non-precious metal catalysts. Incorporation of Fe can notably optimize the electronic structure of the NiOOH active center, decrease the OER overpotential, and its activity in an alkaline medium can be comparable to that of precious metal Ir/Ru-based catalysts;[8] (2) This research aims to develop a high-performance and cost-effective AEMWE system. NiFe LDH is inexpensive, straightforward to prepare, and can maintain excellent stability at high current densities (>500 $mA \cdot cm^{-2}$), which fully satisfies the target operating conditions of our

AEMWE tests. Therefore, homemade NiFe-LDH was used as the anode catalyst; (3) Hydrothermal method was adopted for in-situ growth.[5] This approach ensures that the electrode possesses excellent mechanical stability and rapid charge/gas transfer capability, circumventing the additional resistance introduced by using binders in commercial powder catalysts.

In AEMWE, suitable substrates were chosen according to the distinct working environments of the anode and the cathode.[9] Regarding the cathode, (1) porous carbon paper exhibits chemical stability in an alkaline environment at the cathode potential and does not experience severe corrosion; (2) carbon paper possesses excellent electrical conductivity, high porosity, and good mechanical strength; (3) its planar structure enables close contact with the electrode coated with catalyst slurry, thereby reducing contact resistance. Regarding the anode, (1) Ni-foam demonstrates outstanding electrochemical stability and anti-oxidation corrosion resistance within the alkaline oxygen evolution reaction (OER) potential range; (2) its three-dimensional porous structure offers pathways for the swift escape of oxygen bubbles under high current densities, thereby notably reducing the gas resistance overpotential; (3) its high electrical conductivity and rigidity guarantee uniform current distribution and mechanical support. Carbon paper is not employed for the anode as it experiences corrosion at high OER potentials, which results in performance deterioration and contamination by impurity ions.

Computational methods

All DFT calculations including geometry optimization, electronic structure analysis and adiabatic MD, are performed using the Vienna ab initio Simulation Package (VASP).[10] The exchange-correlation interactions are described using the Perdew-Burke-Ernzerhof (PBE) functional.[11] The interactions between the valence electrons and ionic cores are treated via the projector augmented wave (PAW) method.[12] The van der Waals (vdW) interactions are described using the Grimme DFT-D3 method.[13] The energy cutoff of the plane wave is set to 400 eV. The Pt_{NCs}@NDC and Pt_{NCs}-Pr_{SAs}@NDC slab models are constructed based on the experimental results of the EXAFS spectra. The vacuum layer between slabs is set to more than

15.0 Å. A 1 × 1 × 1 Γ-centered Monkhorst-Pack k-point mesh is used during the geometry optimization. A denser 2 × 2 × 1 k-mesh is employed to characterize the electronic structure. To accurately treat the strong correlation interactions between *d* and *f* electrons, we use the DFT+U method to describe the local properties of Pt 5*d* orbitals (U = 3.2 eV)[14] and Pr 4*f* orbitals (U = 4.5 eV).[15] The COHP analysis is performed by using the LOBSTER software.[16,17] After the geometry optimization, we perform the 1 ps simulated annealing with a 1 fs time step and raise the temperature of Pt_{NCs}@NDC and Pt_{NCs}-Pr_{SAs}@NDC to 300 K and 353 K via velocity rescaling, respectively. Next, 6 ps adiabatic microcanonical ensemble (NVE)[18] molecular dynamic (MD)[19] trajectories are generated with a 1 fs time step. The canonically averaged standard deviation of the position of each atom *i* is calculated, $\sigma_i = \sqrt{\langle(\vec{r}_i - \vec{r}_i)^2\rangle}$, where $\vec{r}_i$ represents the location of atom *i* at time t along the 6 ps MD trajectories.[20] The standard deviation with a smaller value indicates reduced atomic fluctuation.[21] The transition state for water dissociation is determined using the Climbing-Image-Nudged Elastic Band (CI-NEB) method.[22]

For structures with adsorbed H_2O and OH_{ads}, the adsorption energies can be calculated using the following expression:

$$E_{ads} = E_{total} - E_{slab} - E_{H_2O/OH} \quad (5)$$

Where E_{total} and E_{slab} represent the total energies of the surface with and without H_2O or OH_{ads} adsorbate, respectively. $E_{H_2O/OH}$ is the energy of the H_2O molecule or OH_{ads}.

Supplementary Figures

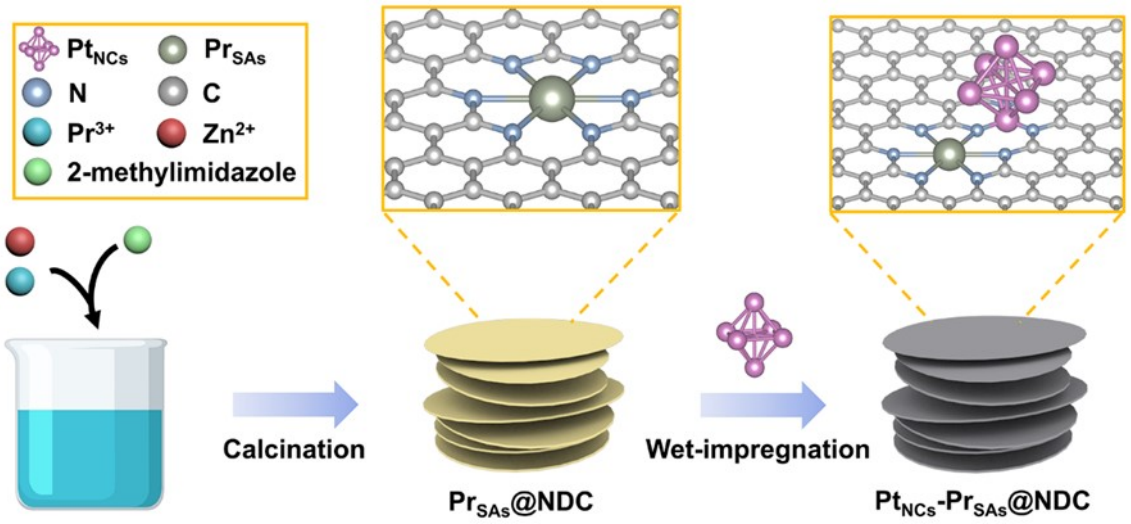

Fig. S1 Synthetic scheme of Pt_{NCs}-Pr_{SAs}@NDC.

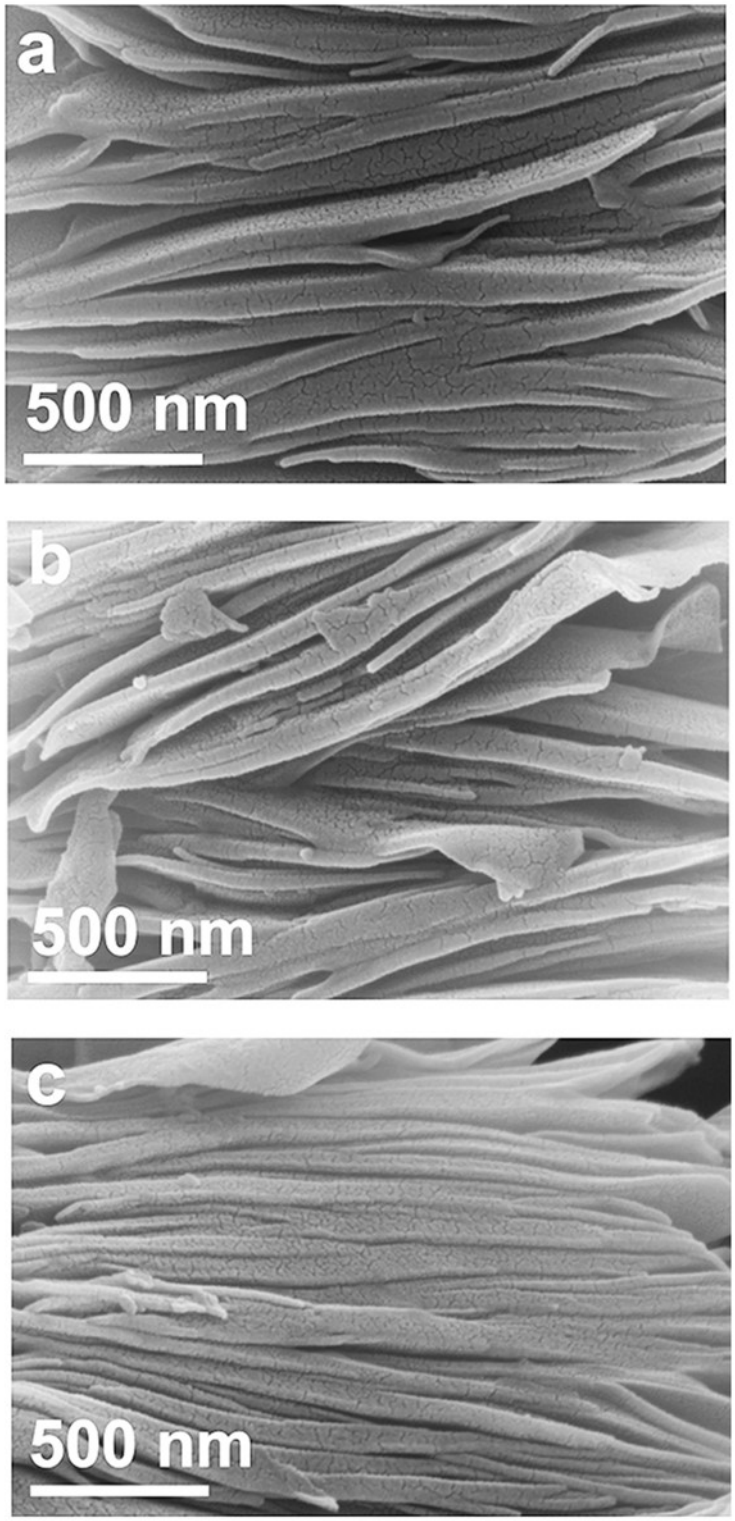

Fig. S2 SEM images of (a) Pt_{NCs}-Pr_{SAs}@NDC, (b) Pt_{NCs}@NDC, and (c) Pr_{SAs}@NDC.

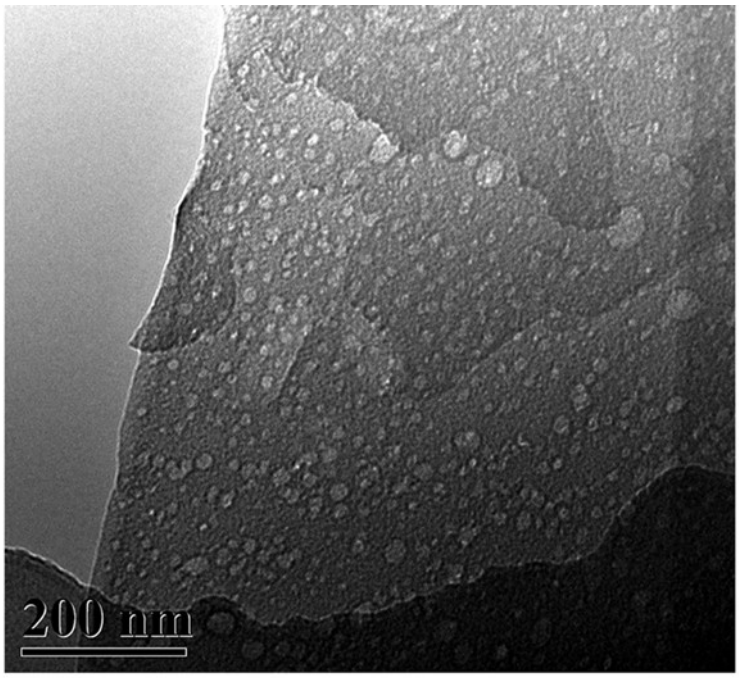

Fig. S3 TEM image of Pt_{NCs}-Pr_{SAs}@NDC.

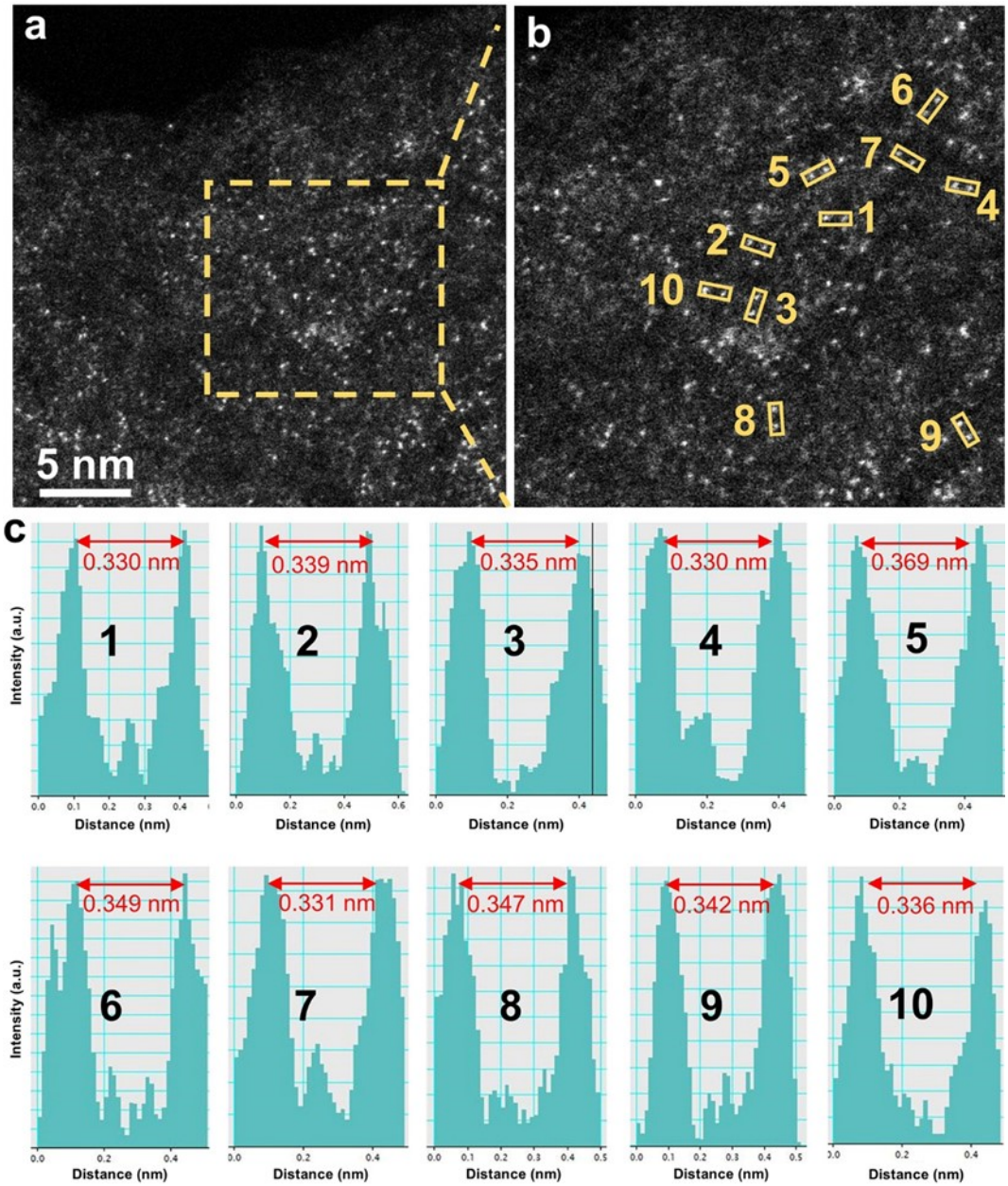

Fig. S4 (a, b) HAADF-STEM image of Pr_{SAs}@NDC and locally magnified image. (c) The intensity profile of Pr_{SAs} obtained following the yellow line in (b).

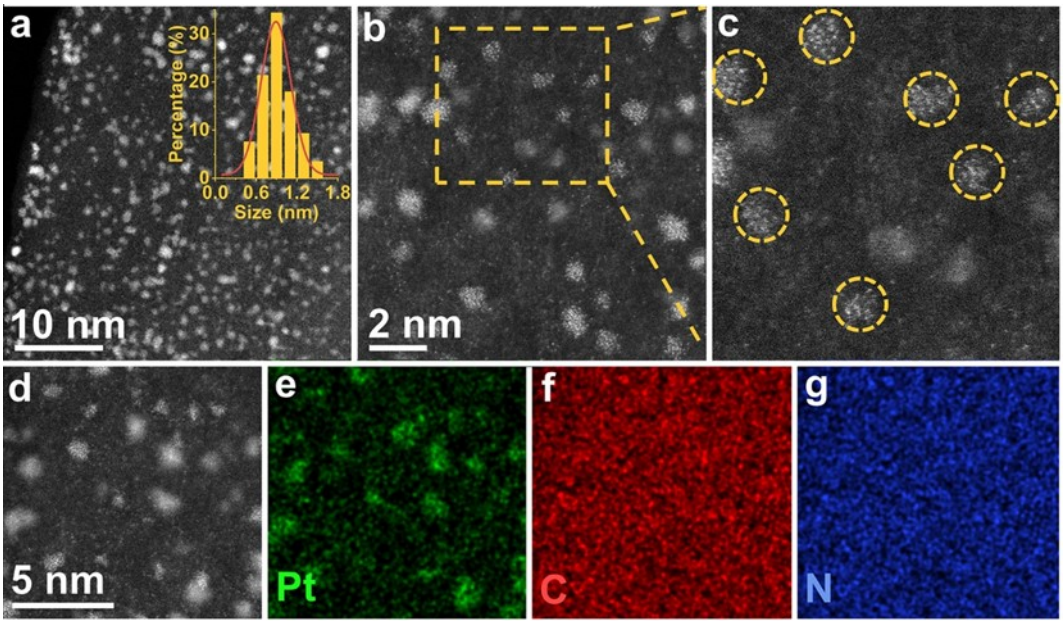

Fig. S5 (a, b) HAADF-STEM images of Pt_{NCs}@NDC. *Inset*, the size distribution of Pt_{NCs}. (c) Locally magnified image of (b). (d) HAADF-STEM and corresponding EDS mapping images of Pt_{NCs}@NDC.

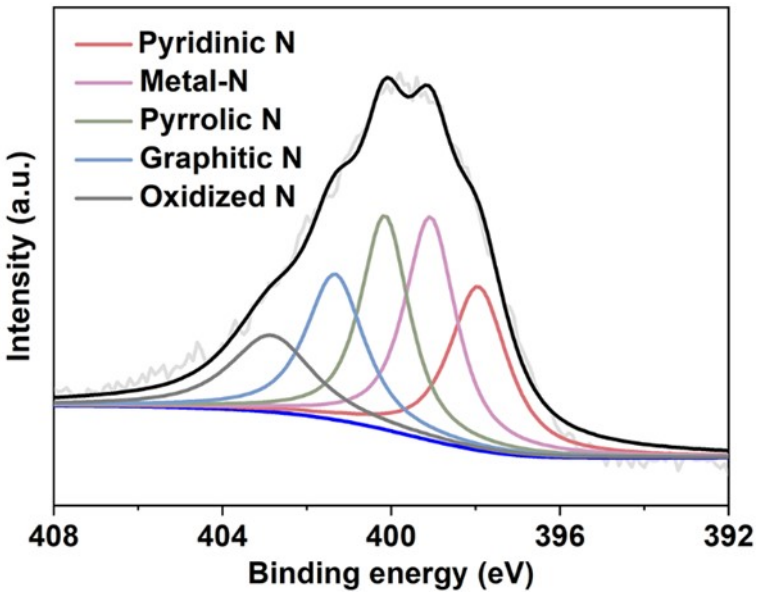

Fig. S6 XPS spectrum of N 1*s* in Pt_{NCs}-Pr_{SAs}@NDC.

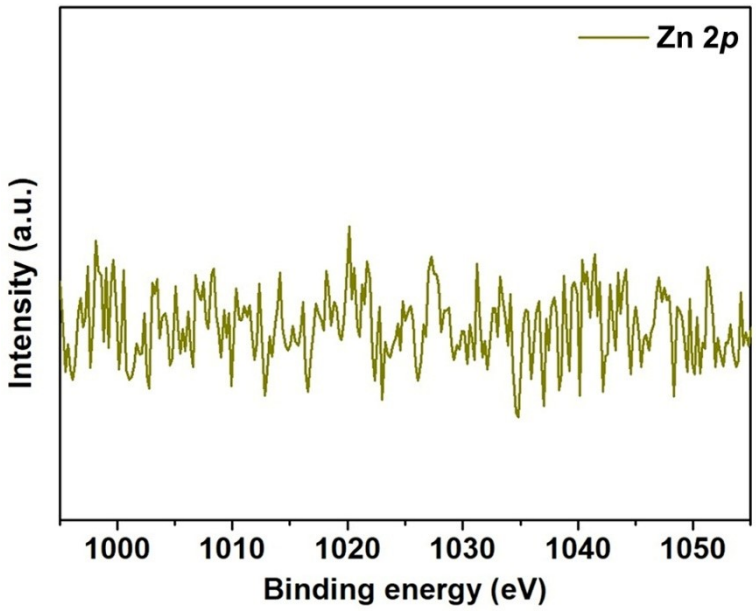

Fig. S7 Zn 2*p* XPS spectrum for Pt_{NCs}-Pr_{SAs}@NDC.

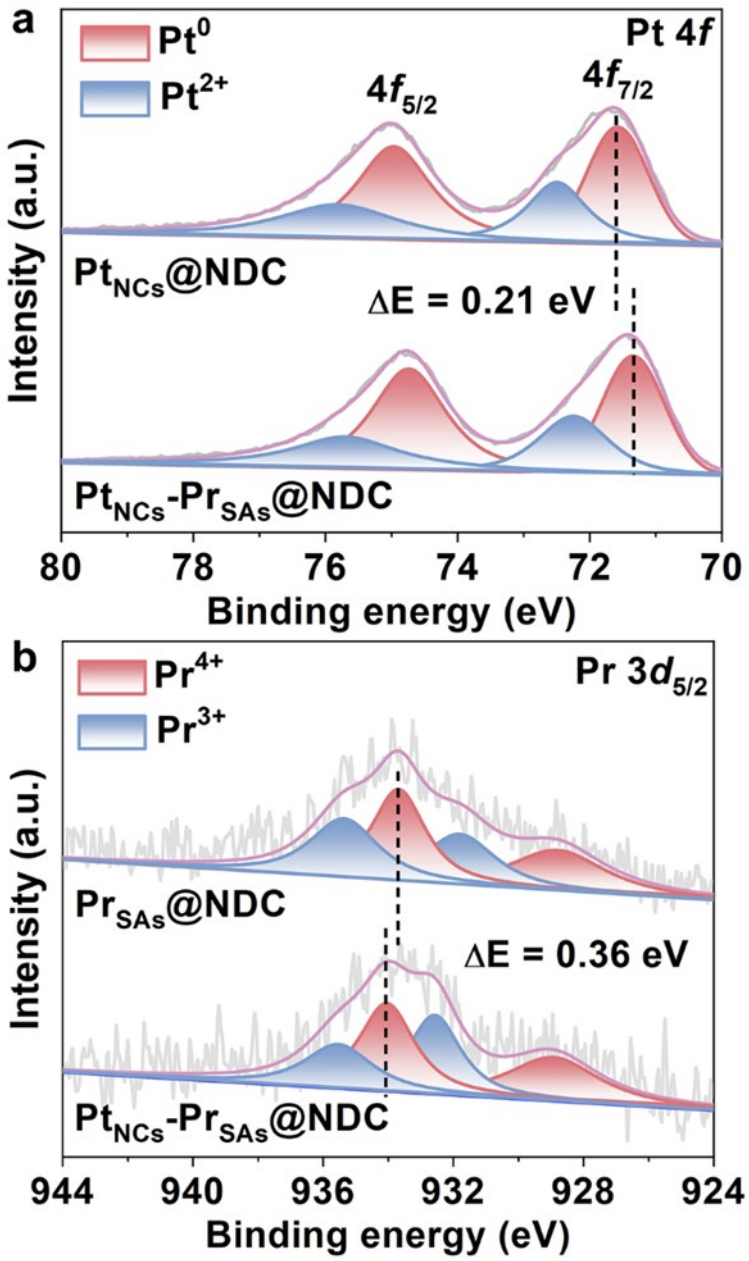

Fig. S8 XPS spectra of (a) Pt 4*f* and (b) Pr $3d_{5/2}$ in different samples.

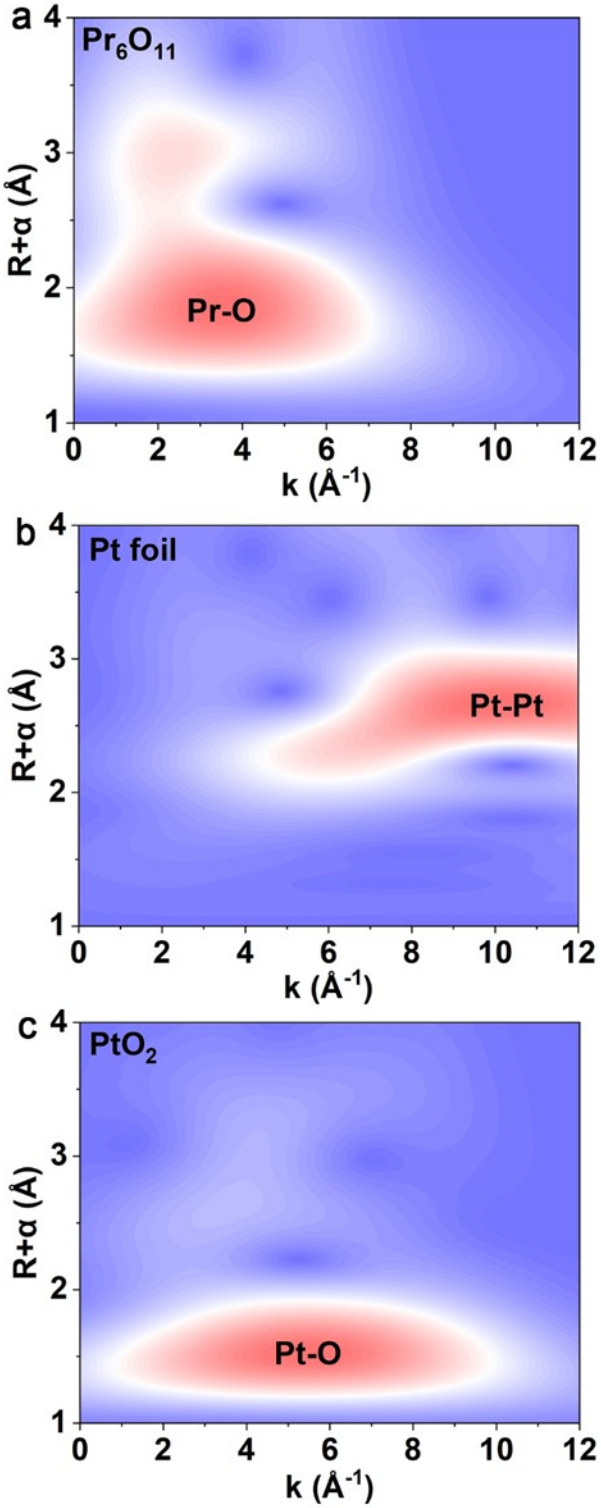

Fig. S9 Wavelet transforms of the EXAFS spectra of (a) Pr_6O_{11}, (b) Pt foil, and (c) PtO_2.

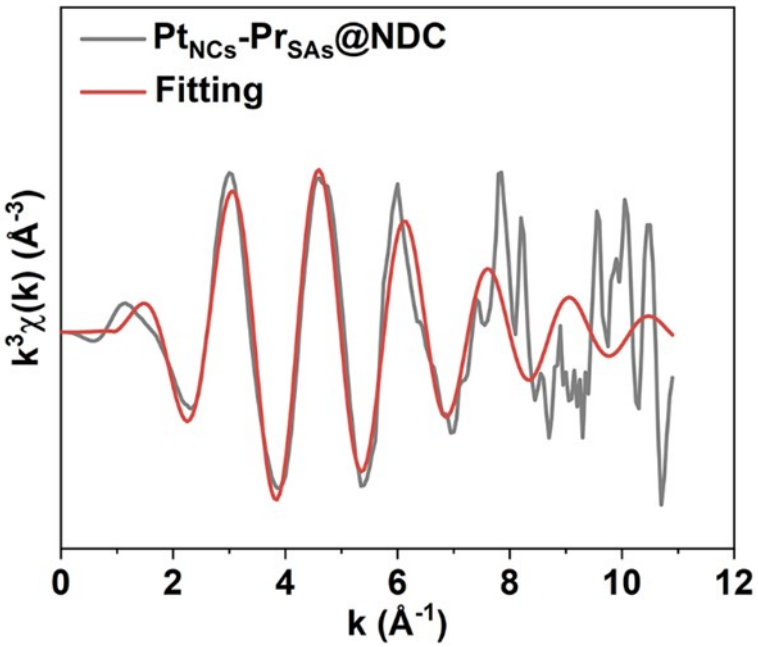

Fig. S10 Fourier-transformed magnitude of Pr L_3 EXAFS spectra in k space of Pt_{NCs}-Pr_{SAs}@NDC.

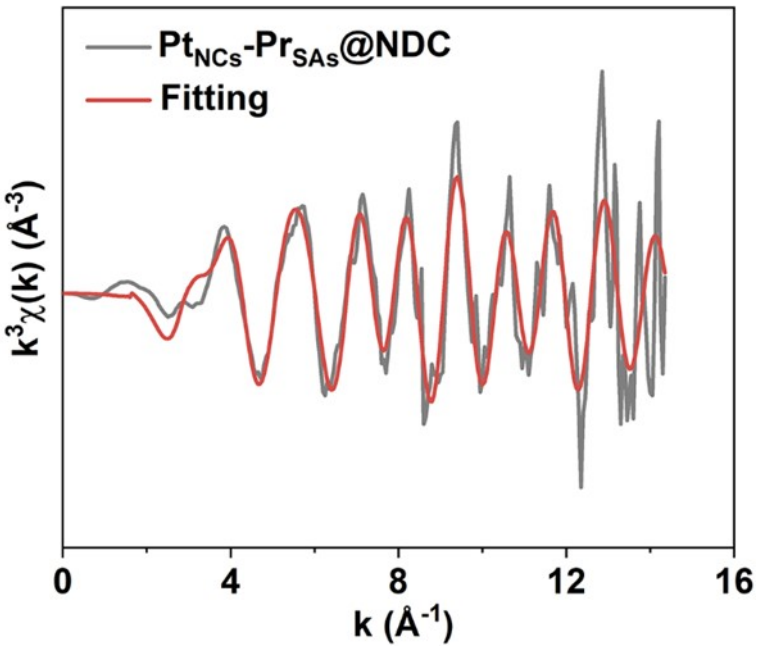

Fig. S11 Fourier-transformed magnitude of Pt L_3 EXAFS spectra in k space of Pt_{NCs}-Pr_{SAs}@NDC.

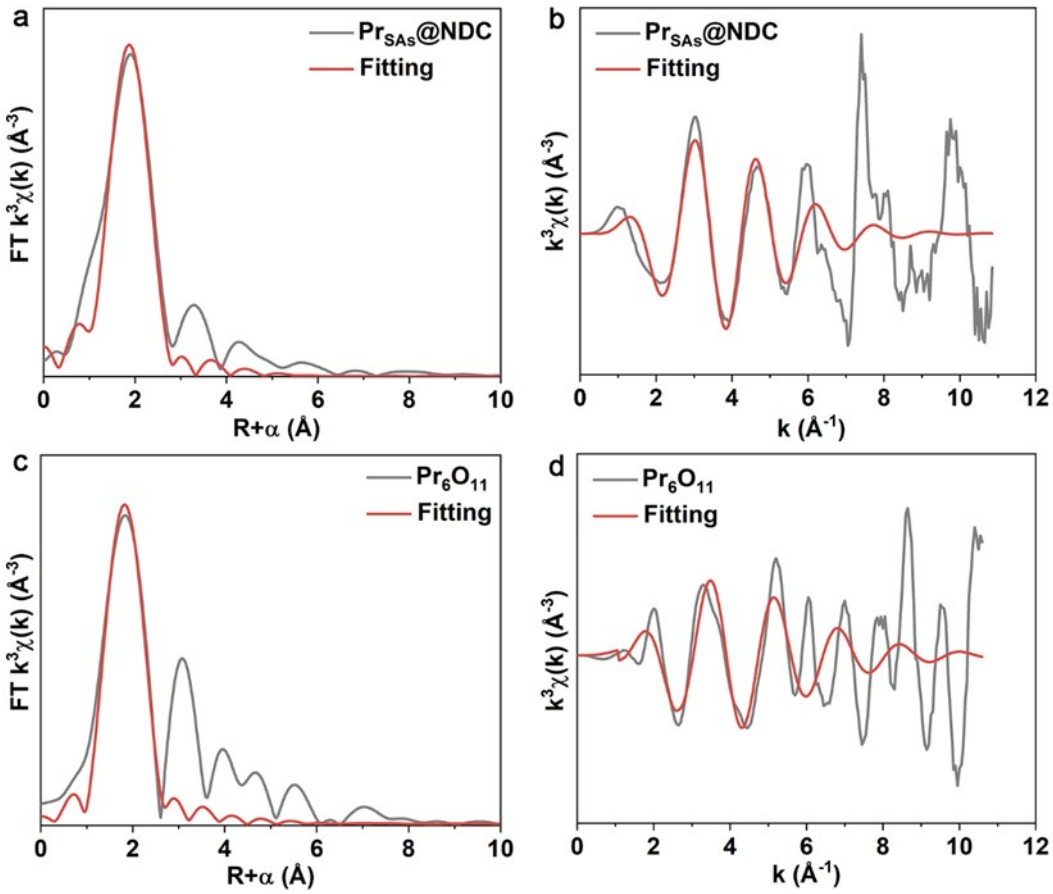

Fig. S12 Fourier-transformed magnitude of Pr L_3 EXAFS spectra in the R space and k space of (a, b) Pr_{SAs}@NDC and (c, d) Pr_6O_{11}.

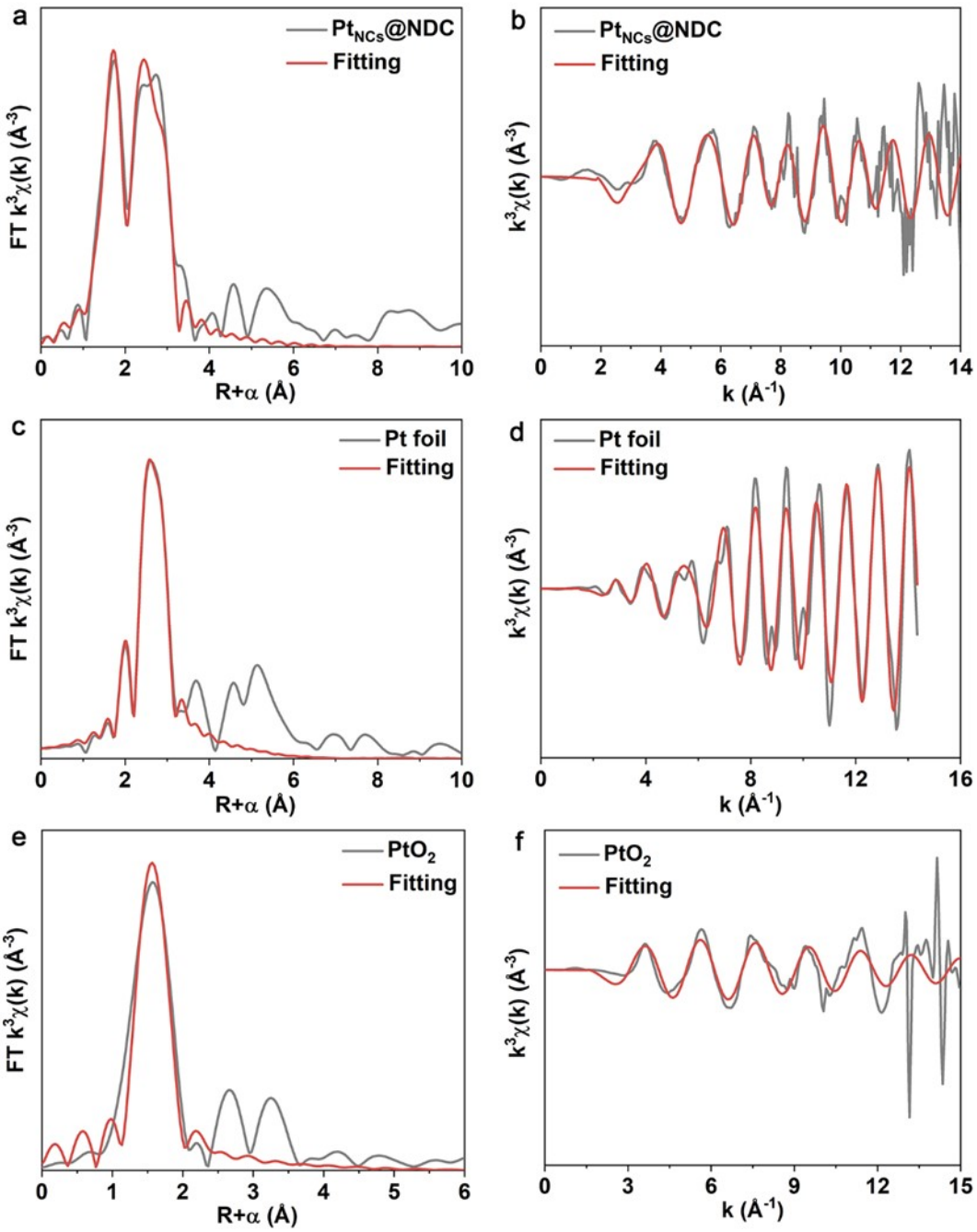

Fig. S13 Fourier-transformed magnitude of Pt L_3 EXAFS spectra in the R space and k space of (a, b) Pt_{NCs}@NDC, (c, d) Pt foil, and (e, f) PtO_2.

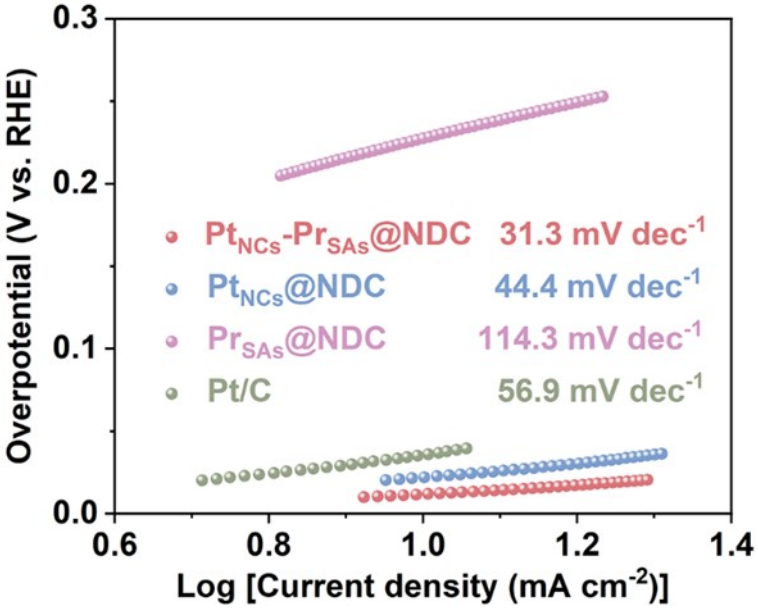

Fig. S14 Tafel slopes of Pt_{NCs}-Pr_{SAs}@NDC, Pt_{NCs}@NDC, Pr_{SAs}@NDC, and commercial Pt/C.

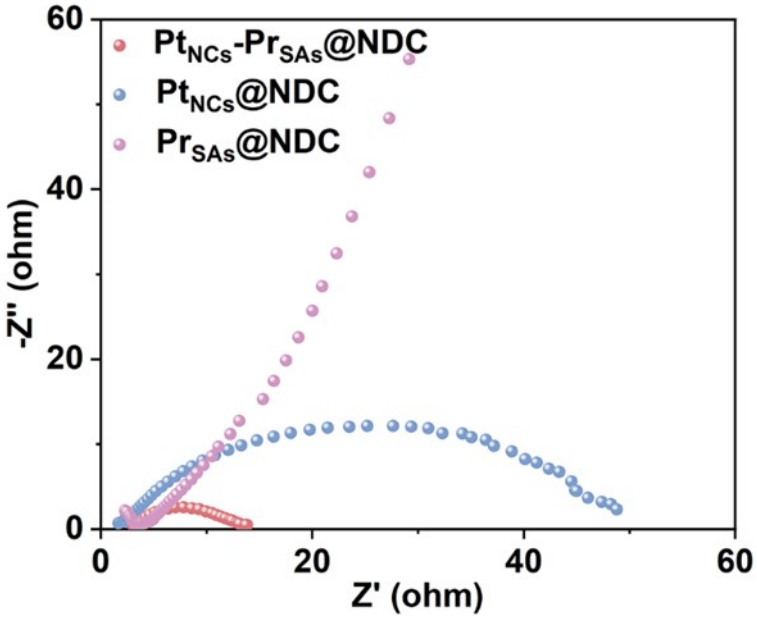

Fig. S15 Nyquist plots measured at -0.94 V (vs. RHE) for Pt_{NCs}-Pr_{SAs}@NDC, Pt_{NCs}@NDC, and Pr_{SAs}@NDC. The fitting results are shown in Table S13.

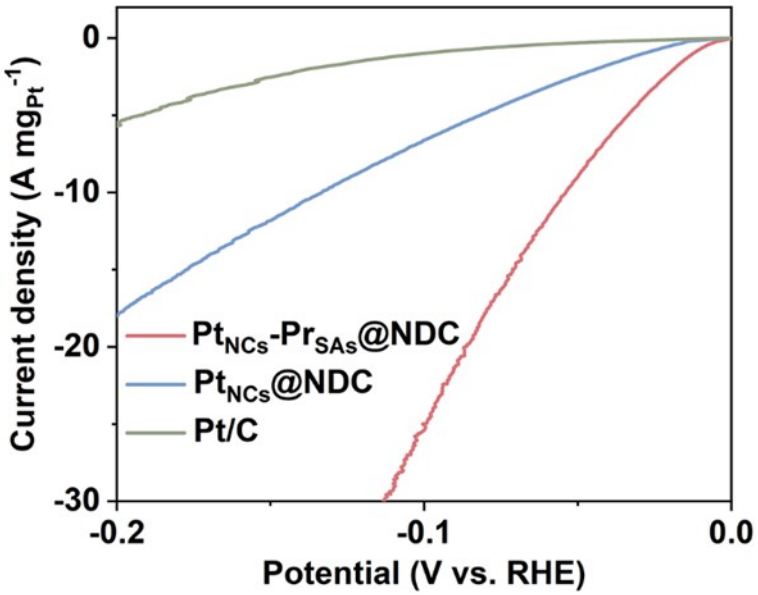

Fig. S16 LSV curves of Pt_{NCs}-Pr_{SAs}@NDC, Pt_{NCs}@NDC, and commercial Pt/C normalized by actual noble metal (Pt) mass in 1.0 M KOH solution.

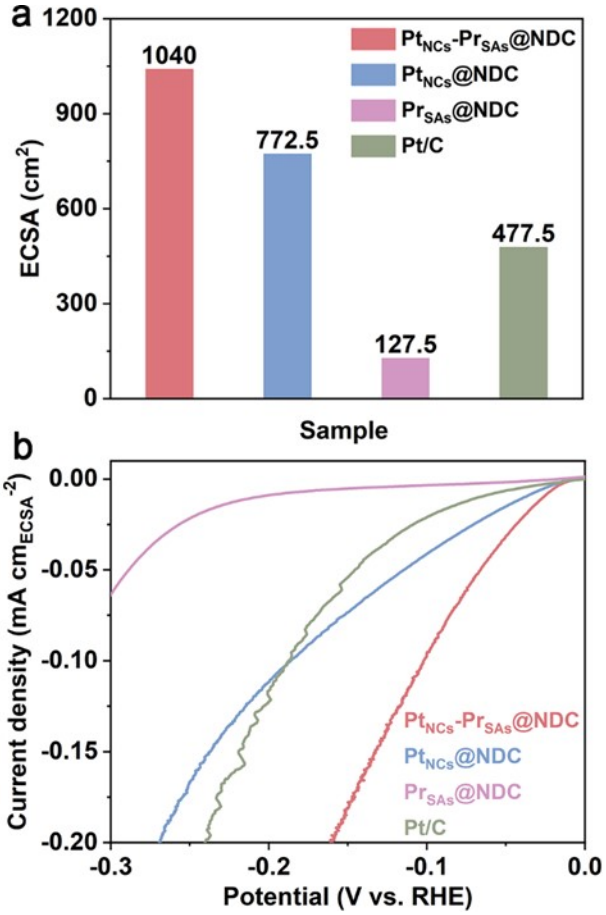

Fig. S17 (a) ECSAs of Pt_{NCs}-Pr_{SAs}@NDC, Pt_{NCs}@NDC, Pr_{SAs}@NDC, and commercial Pt/C, respectively. (b) HER polarization curves normalized by ECSA for Pt_{NCs}-Pr_{SAs}@NDC, Pt_{NCs}@NDC, Pr_{SAs}@NDC, and commercial Pt/C, respectively.

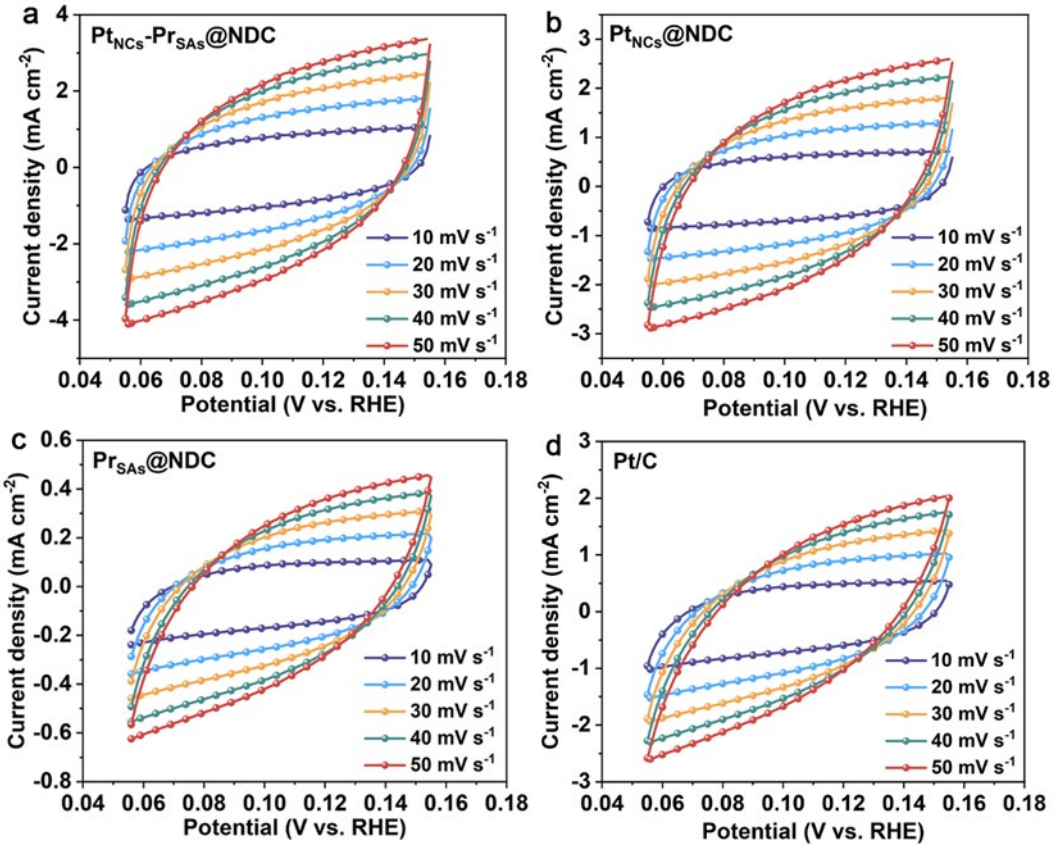

Fig. S18 Cyclic voltammograms of (a) Pt_{NCs}-Pr_{SAs}@NDC, (b) Pt_{NCs}@NDC, (c) Pr_{SAs}@NDC, and (d) commercial Pt/C in the double layer region (without Faradic process) at scan rates of 10, 20, 30, 40, and 50 mV·s^{-1}.

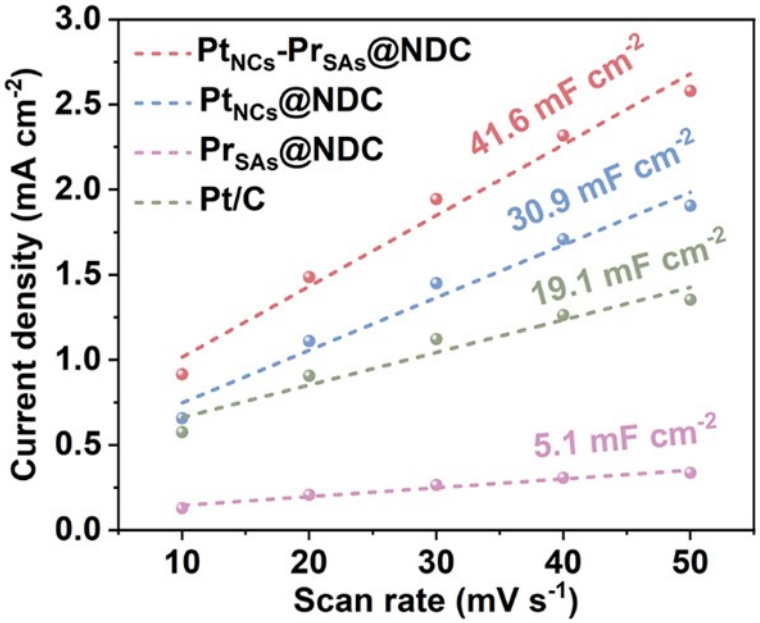

Fig. S19 Double-layer capacitance C_{dl} of Pt_{NCs}-Pr_{SAs}@NDC, Pt_{NCs}@NDC, Pr_{SAs}@NDC, and commercial Pt/C, respectively.

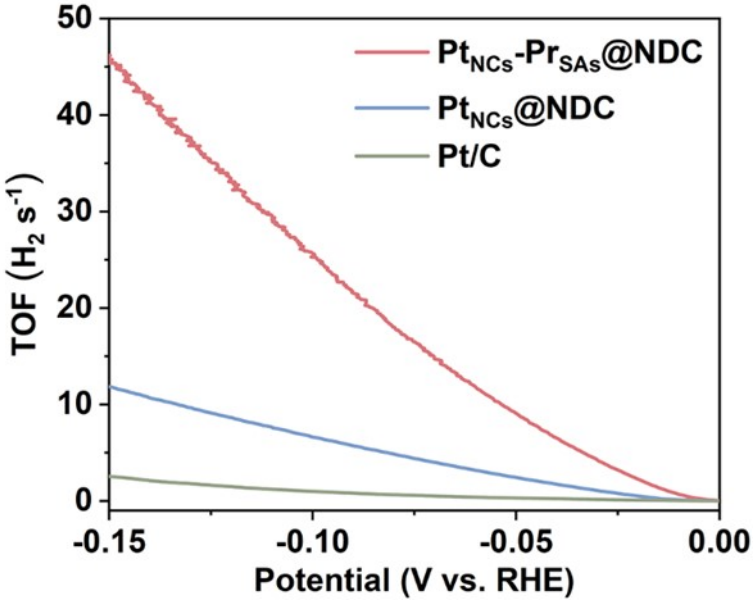

Fig. S20 TOF curves of Pt_{NCs}-Pr_{SAs}@NDC, Pt_{NCs}@NDC, and commercial Pt/C.

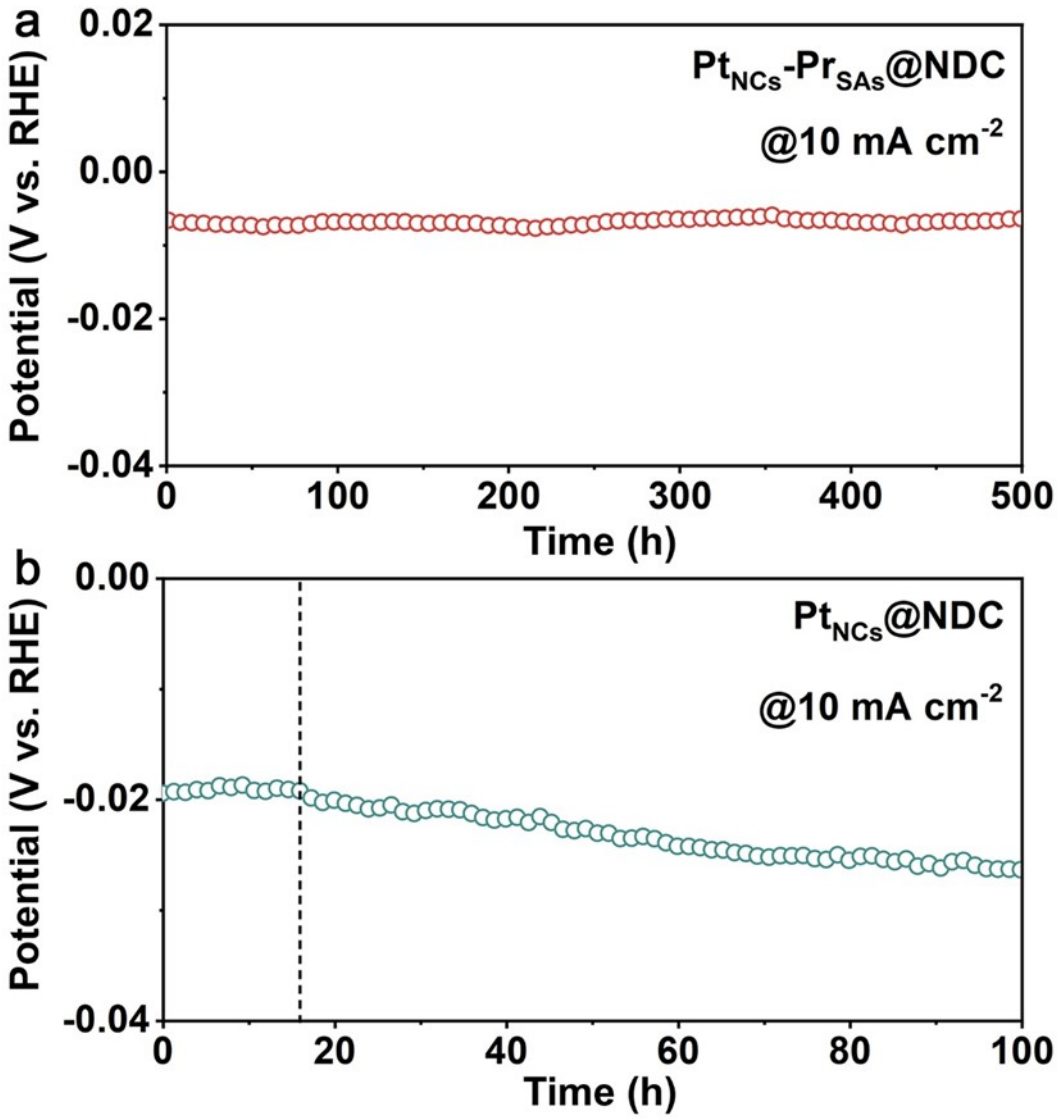

Fig. S21 Chronopotentiometry curves of (a) Pt_{NCs}-Pr_{SAs}@NDC and (b) Pt_{NCs}@NDC at 10 mA·cm^{-2}.

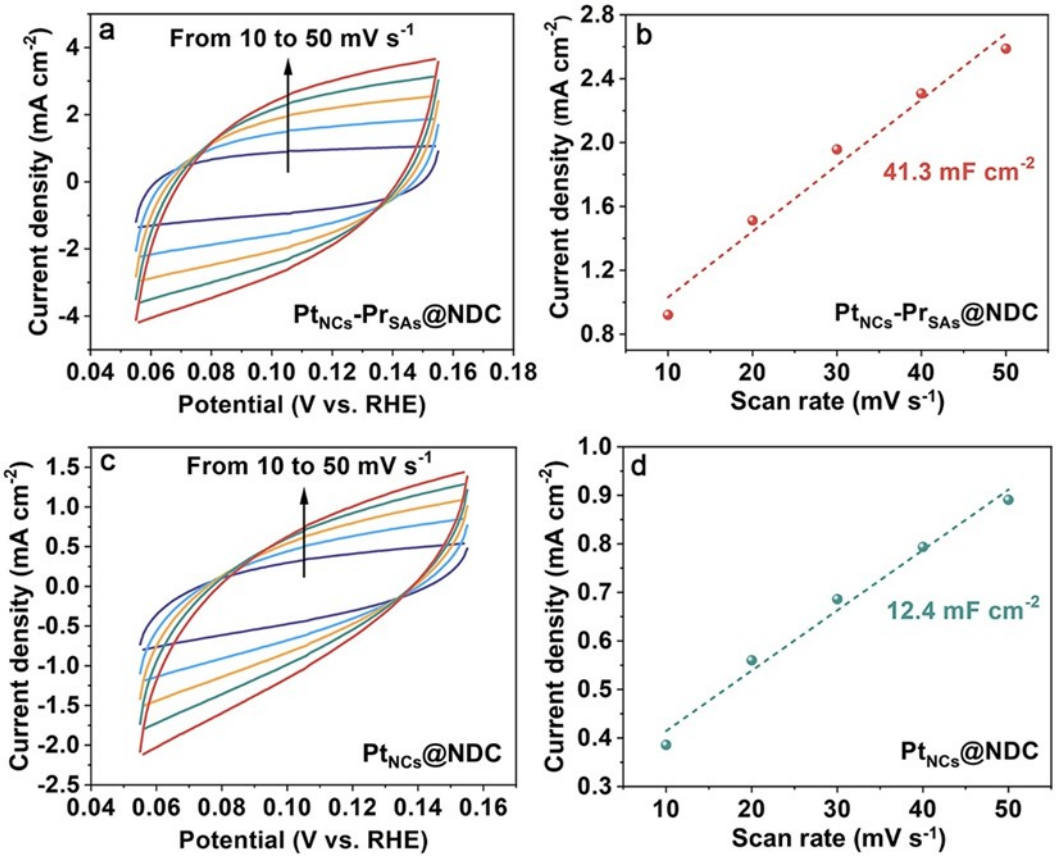

Fig. S22 Cyclic voltammograms after stability tests of (a) Pt_{NCs}-Pr_{SAs}@NDC, (c) Pt_{NCs}@NDC in the double layer region (without Faradic process) at scan rates of 10, 20, 30, 40, and 50 $mV \cdot s^{-1}$. Double-layer capacitance C_{dl} after stability tests of (b) Pt_{NCs}-Pr_{SAs}@NDC and (d) Pt_{NCs}@NDC.

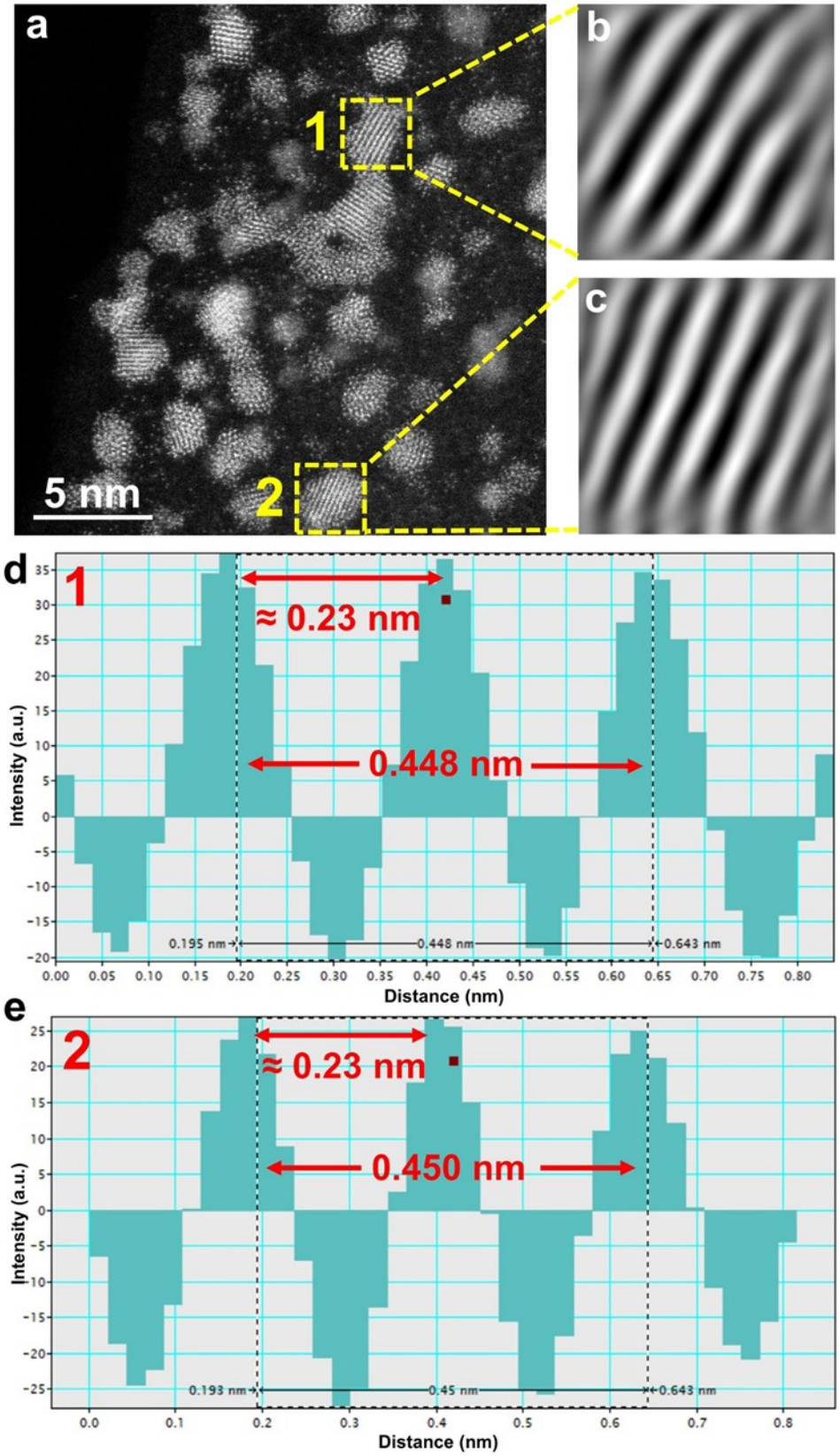

Fig. S23 (a) HAADF-STEM image of the Pt_{NCs}@NDC catalyst after the stability test, the lattice spacing corresponding to the marked area of (b) 1 and (c) 2, and intensity profile corresponding to the marked area of (d) 1 and (e) 2.

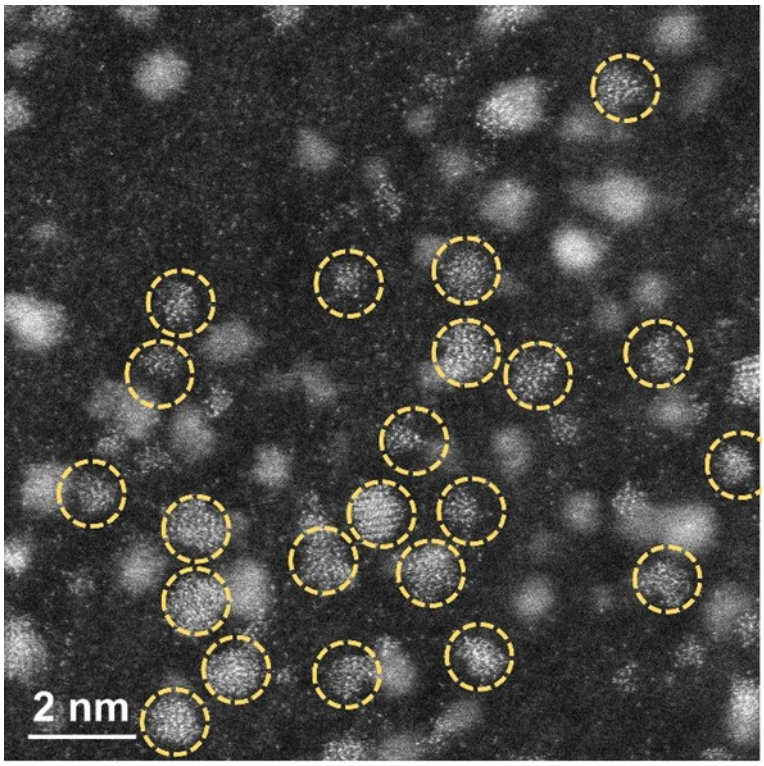

Fig. S24 HAADF-STEM image of the Pt_{NCs}-Pr_{SAs}@NDC catalyst after the stability test. The Pt_{NCs} are marked by yellow circles.

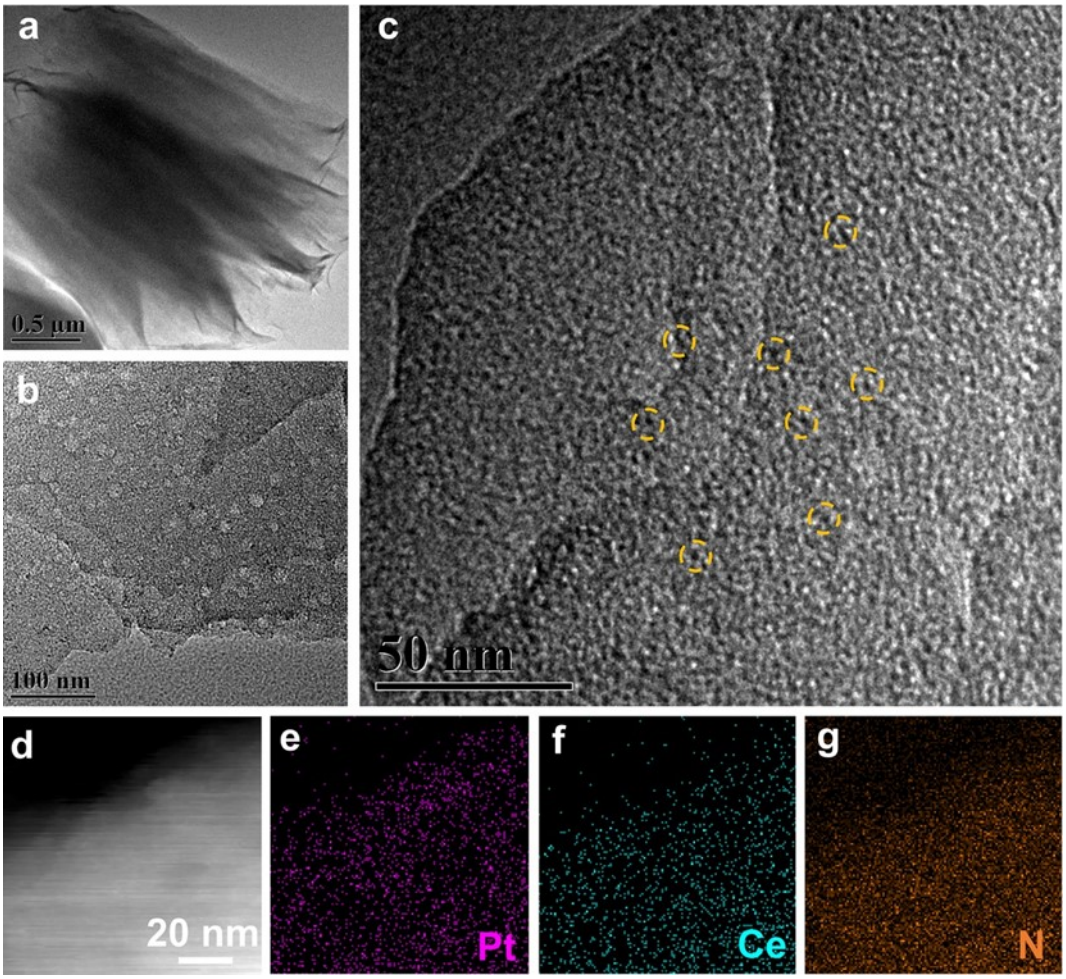

Fig. S25 (a-c) TEM images of Pt_{NCs}-Ce_{SAs}@NDC. Yellow circles mark some of the Pt_{NCs}. (d) HAADF-STEM image and corresponding EDS mapping of (e) Pt, (f) Ce, and (g) N in Pt_{NCs}-Ce_{SAs}@NDC.

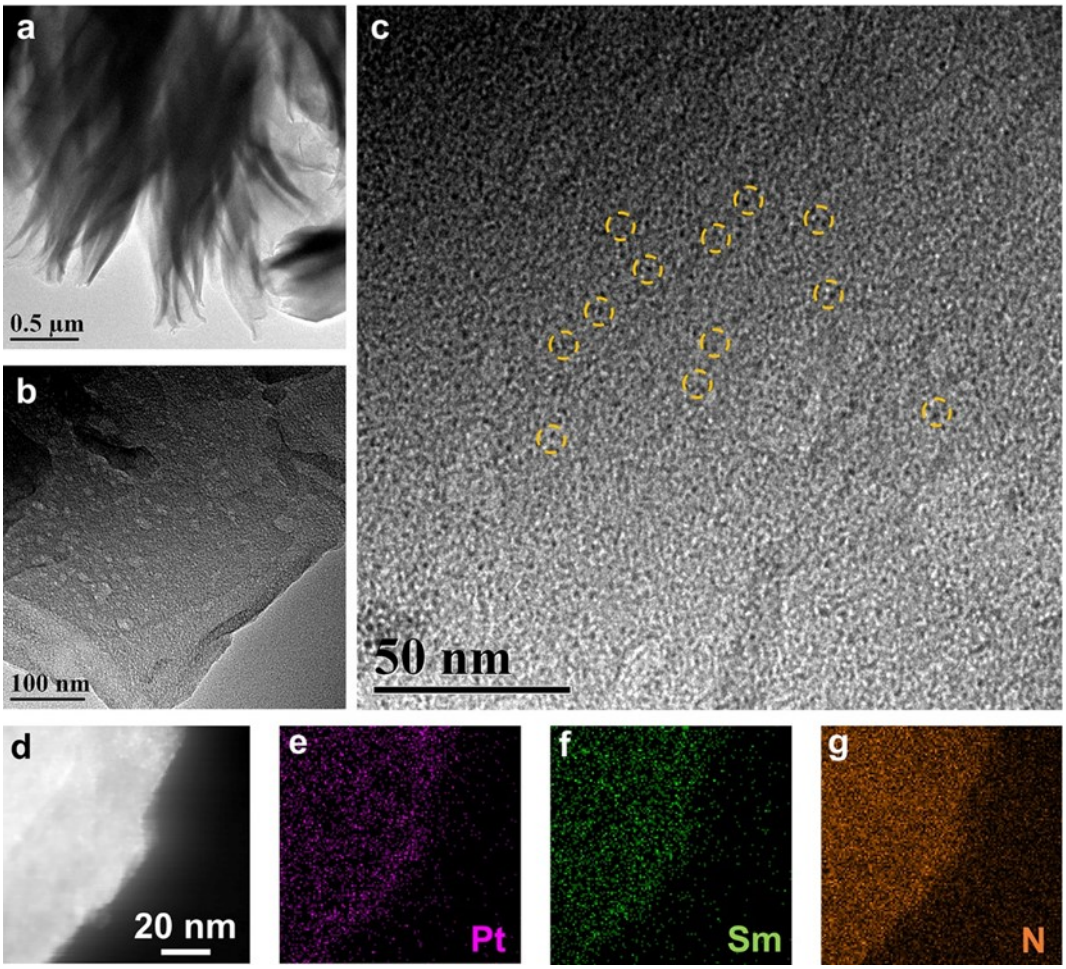

Fig. S26 (a-c) TEM images of Pt_{NCs}-Sm_{SAs}@NDC. Yellow circles mark some of the Pt_{NCs}. (d) HAADF-STEM image and corresponding EDS mapping of (e) Pt, (f) Sm, and (g) N in Pt_{NCs}-Sm_{SAs}@NDC.

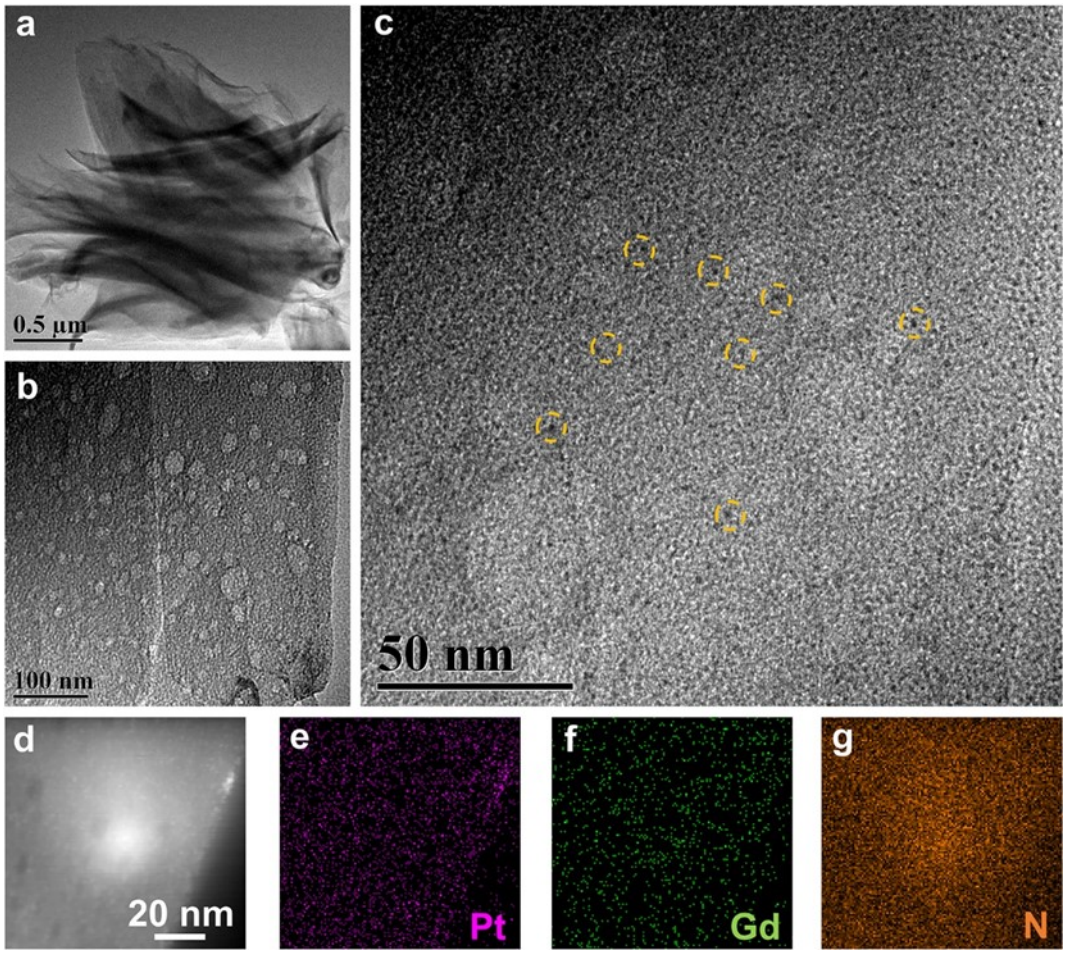

Fig. S27 (a-c) TEM images of Pt_{NCs}-Gd_{SAs}@NDC. Yellow circles mark some of the Pt_{NCs}. (d) HAADF-STEM image and corresponding EDS mapping of (e) Pt, (f) Gd, and (g) N in Pt_{NCs}-Gd_{SAs}@NDC.

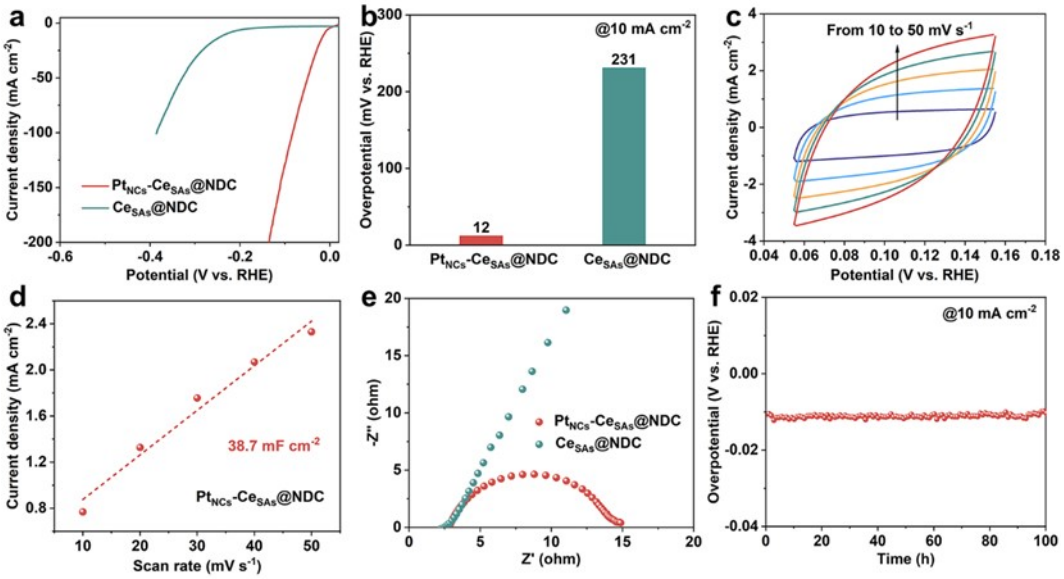

Fig. S28 (a) LSV curves. (b) Comparison of overpotentials of catalysts. (c) Pt_{NCs}-Ce_{SAs}@NDC in the double layer region (without Faradic process) at scan rates of 10, 20, 30, 40, and 50 $mV \cdot s^{-1}$. (d) Corresponding double-layer capacitance C_{dl} of Pt_{NCs}-Ce_{SAs}@NDC. (e) Nyquist plots measured at -0.94 V (vs. RHE) of Pt_{NCs}-Ce_{SAs}@NDC and Ce_{SAs}@NDC. (f) Chronopotentiometry curves of Pt_{NCs}-Ce_{SAs}@NDC at 10 $mA \cdot cm^{-2}$.

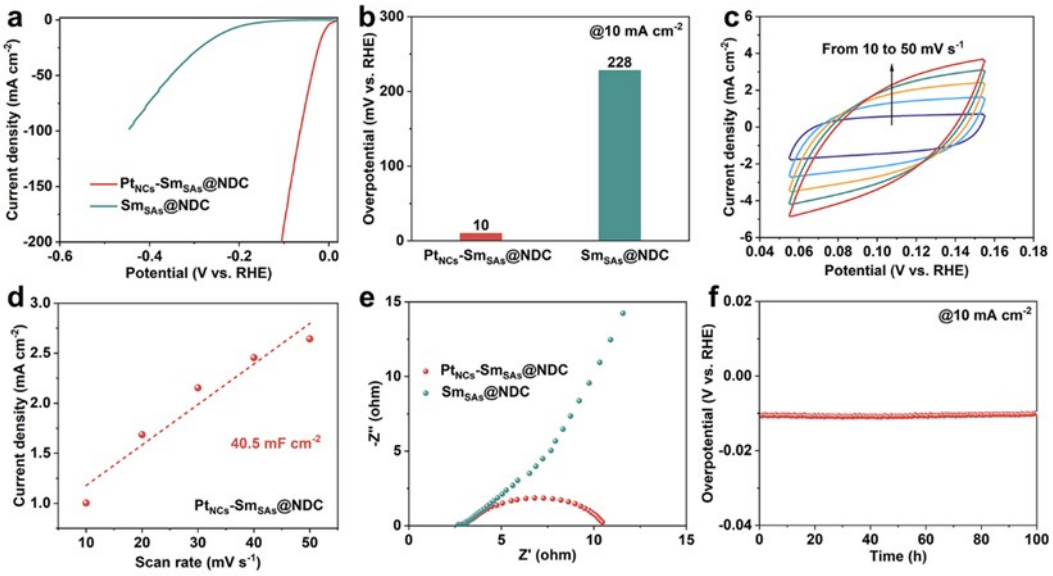

Fig. S29 (a) LSV curves. (b) Comparison of overpotentials of catalysts. (c) Pt_{NCs}-Sm_{SAs}@NDC in the double layer region (without Faradic process) at scan rates of 10, 20, 30, 40, and 50 mV·s^{-1}. (d) Corresponding double-layer capacitance C_{dl} of Pt_{NCs}-Sm_{SAs}@NDC. (e) Nyquist plots measured at -0.94 V (vs. RHE) of Pt_{NCs}-Sm_{SAs}@NDC and Sm_{SAs}@NDC. (f) Chronopotentiometry curves of Pt_{NCs}-Sm_{SAs}@NDC at 10 mA·cm^{-2}.

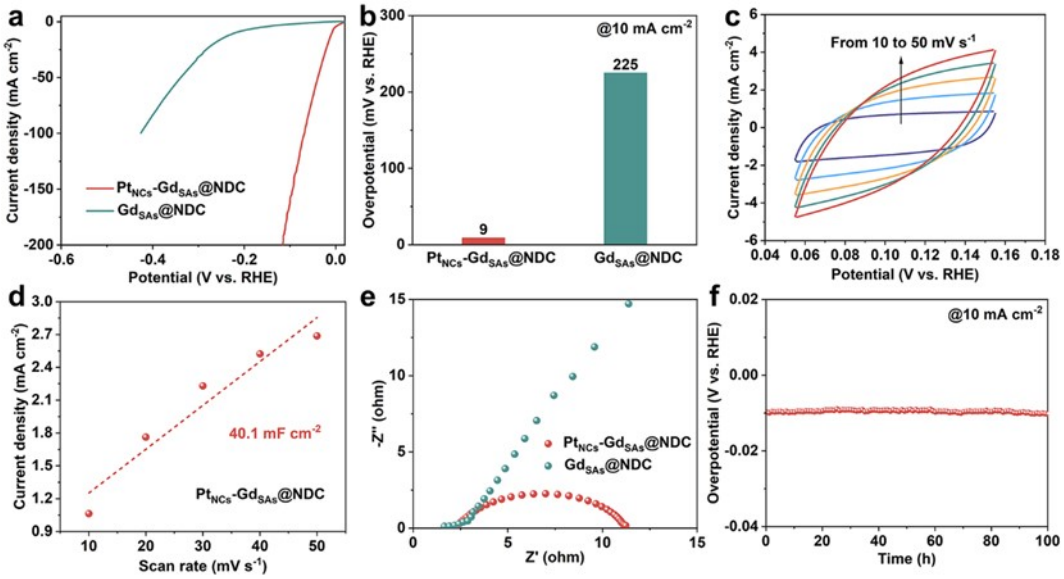

Fig. S30 (a) LSV curves. (b) Comparison of overpotentials of catalysts. (c) Pt_{NCs}-Gd_{SAs}@NDC in the double layer region (without Faradic process) at scan rates of 10, 20, 30, 40, and 50 mV·s^{-1}. (d) Corresponding double-layer capacitance C_{dl} of Pt_{NCs}-Gd_{SAs}@NDC. (e) Nyquist plots measured at -0.94 V (vs. RHE) of Pt_{NCs}-Gd_{SAs}@NDC and Gd_{SAs}@NDC. (f) Chronopotentiometry curves of Pt_{NCs}-Gd_{SAs}@NDC at 10 mA·cm^{-2}.

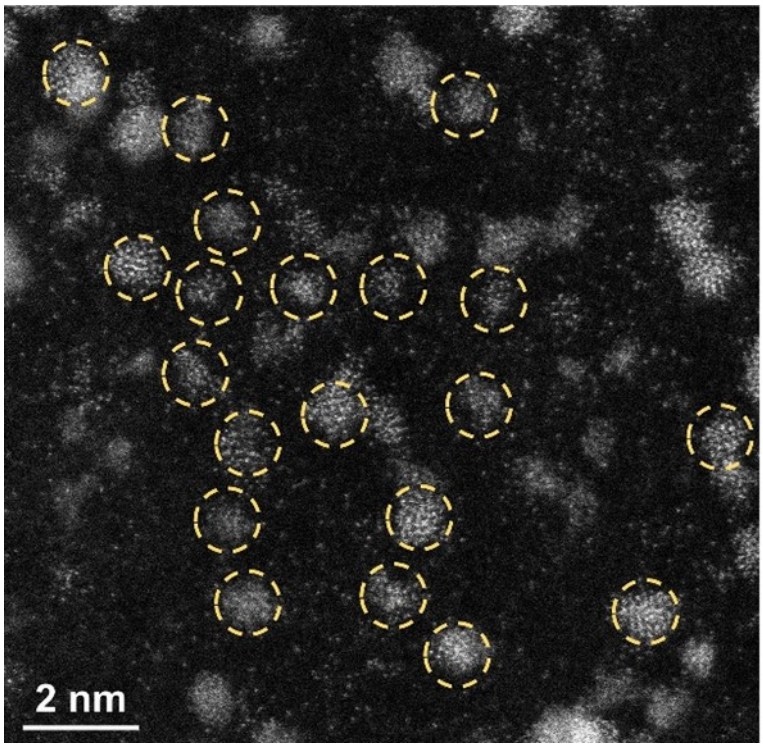

Fig. S31 HAADF-STEM image of the Pt_{NCs}-Pr_{SAs}@NDC catalyst after the high current density stability test. The Pt_{NCs} are marked by yellow circles.

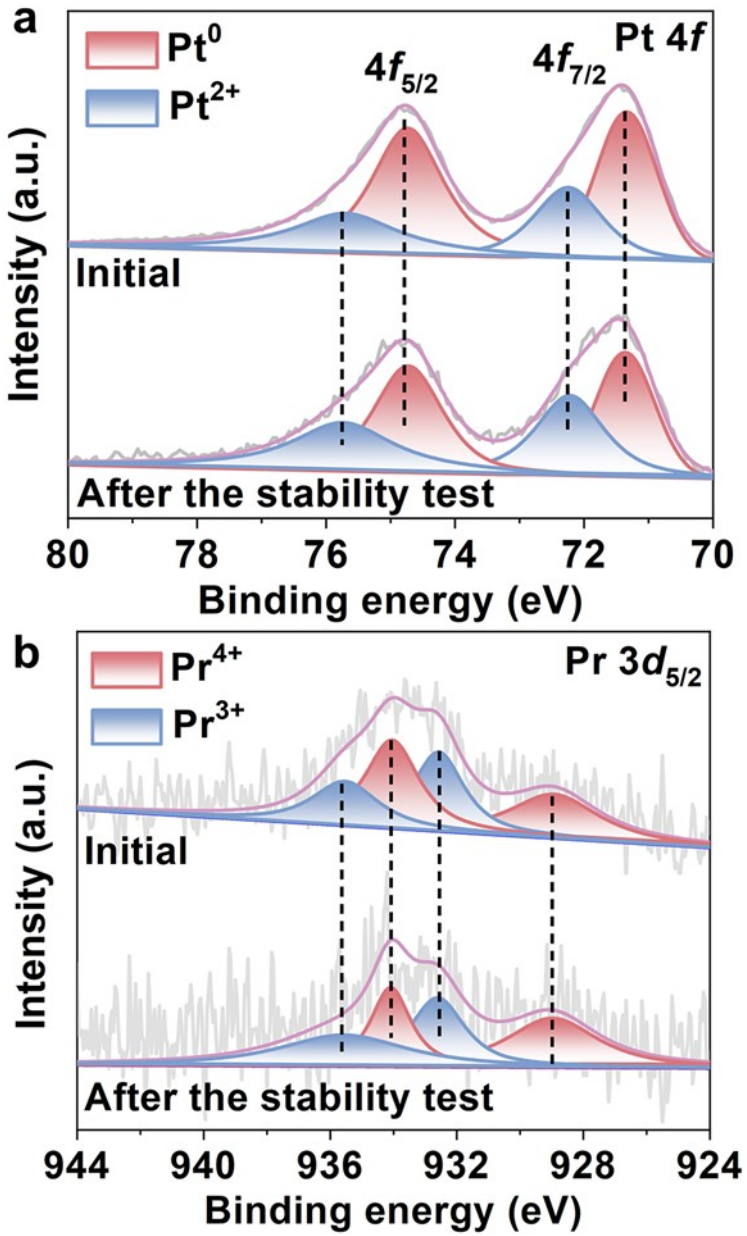

Fig. S32 XPS spectra of Pt 4*f* and Pr 3*d* in Pt_{NCs}-Pr_{SAs}@NDC before and after the high current density stability test.

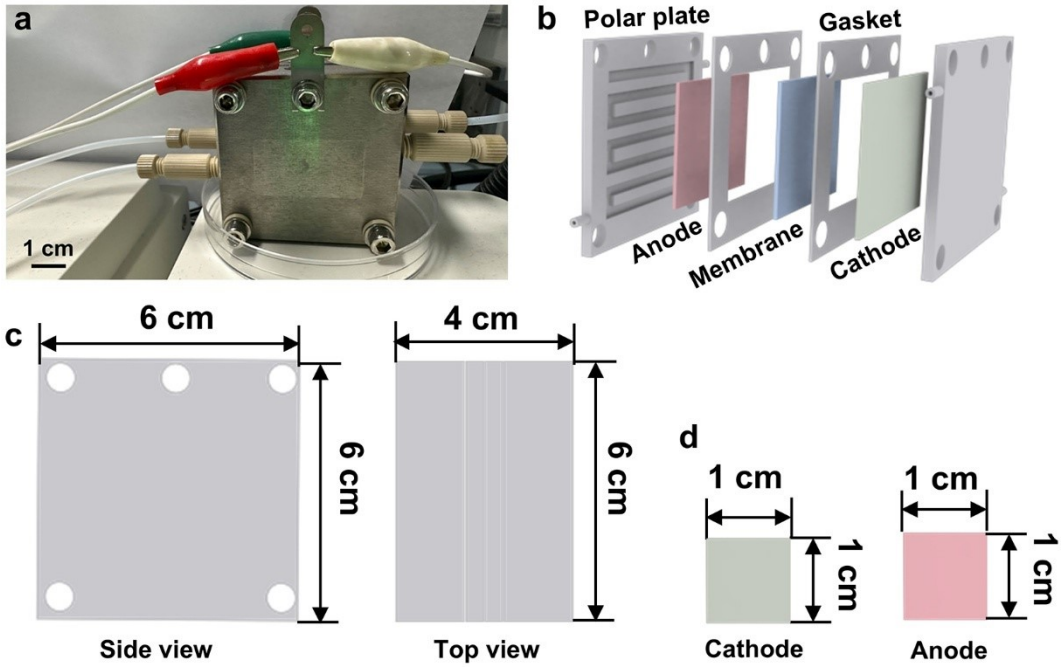

Fig. S33 (a) Photograph and (b) schematic diagram of the AEMWE. (c) The side view and Top view of AEMWE. (d) The dimensional diagram of the cathode and anode of the AEMWE.

As shown in Figure S33, the dimensions of the electrode working area is 1×1 cm^2. The overall dimensions of the AEMWE device are 6×6×4 cm^3 (length×width×height).

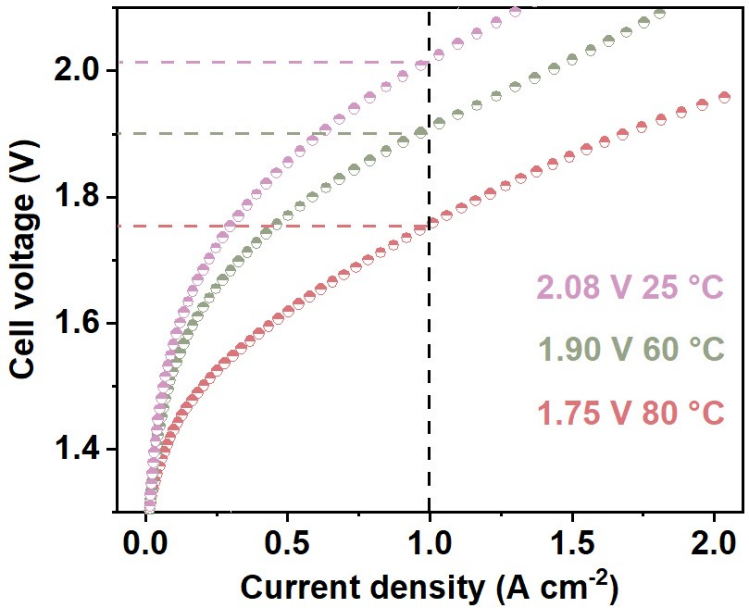

Fig. S34 Performance of Pt_{NCs}-Pr_{SAs}@NDC||NiFe-LDH-based AEMWE at different temperatures.

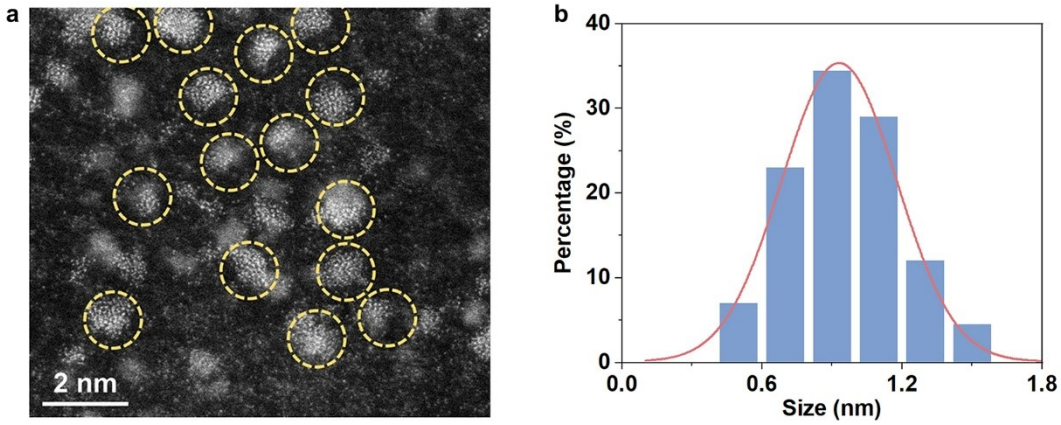

Fig. S35 (a) HAADF-STEM image of the Pt_{NCs}-Pr_{SAs}@NDC catalyst after 500-h electrolysis. The Pt_{NCs} are marked by yellow circles. (b) size distribution of Pt_{NCs}.

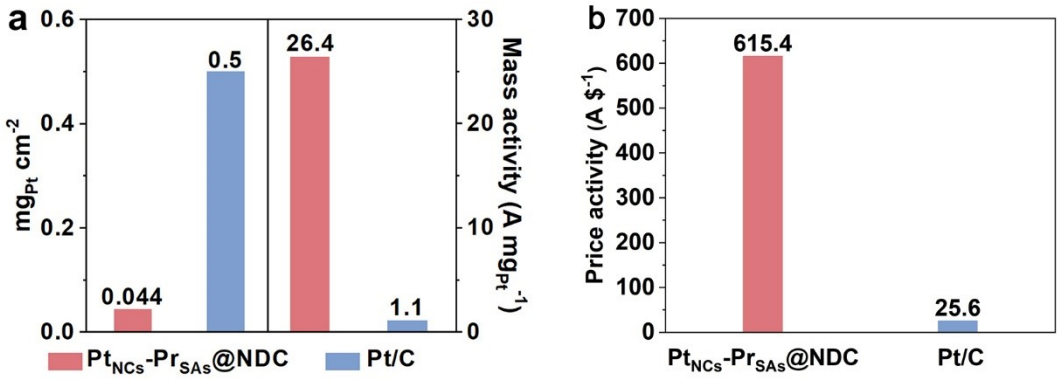

Fig. S36 (a) Comparison of cathode Pt loading and mass activity (1.8 V_{cell}) between Pt_{NCs}-Pr_{SAs}@NDC and commercial Pt/C. (b) Price activities of Pt_{NCs}-Pr_{SAs}@NDC||NiFe-LDH-based AEMWE and Pt/C||NiFe-LDH-based AEMWE at 1.8 V_{cell}.

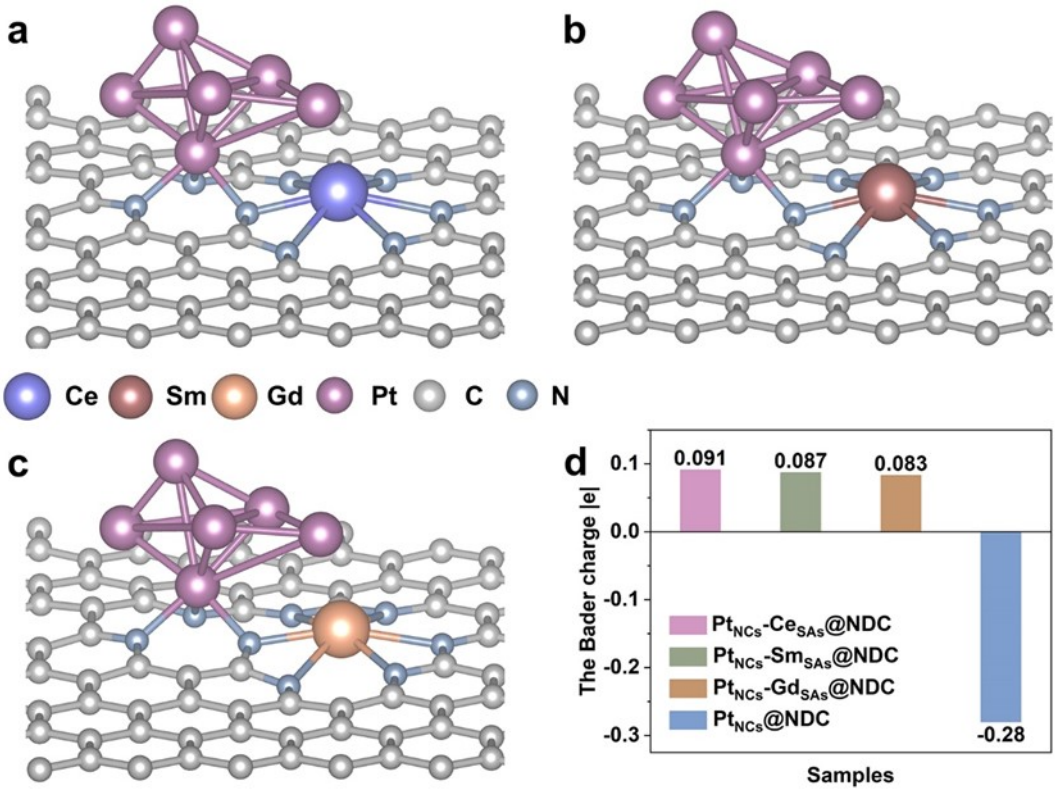

Fig. S37 Atomic structure models of (a) Pt_{NCs}-Ce_{SAs}@NDC, (b) Pt_{NCs}-Sm_{SAs}@NDC, and (c) Pt_{NCs}-Gd_{SAs}@NDC. (d) Bader charge analyses of Pt_{NCs}-Ce_{SAs}@NDC, Pt_{NCs}-Sm_{SAs}@NDC, and Pt_{NCs}-Gd_{SAs}@NDC.

The Bader charge analyses indicate that compared with the electron deficiency on Pt in Pt_{NCs}@NDC due to the 0.28 |e| Pt→N electron transfer, the about 0.091 |e|, 0.087 |e|, and 0.083 |e| RE→Pt electron transferred through the Pt⌒N⌒Pr interfacial electron bridge in Pt_{NCs}-Ce_{SAs}@NDC, Pt_{NCs}-Sm_{SAs}@NDC, and Pt_{NCs}-Gd_{SAs}@NDC, respectively, effectively promotes the charge density at Pt sites, which reduces the charge imbalance of the Pt-N bond. These results indicate that an electron identical transfer mechanism to Pt_{NCs}-Pr_{SAs}@NDC, i.e., RE→Pt. (**Fig. S28-S30**, **Table S10**).

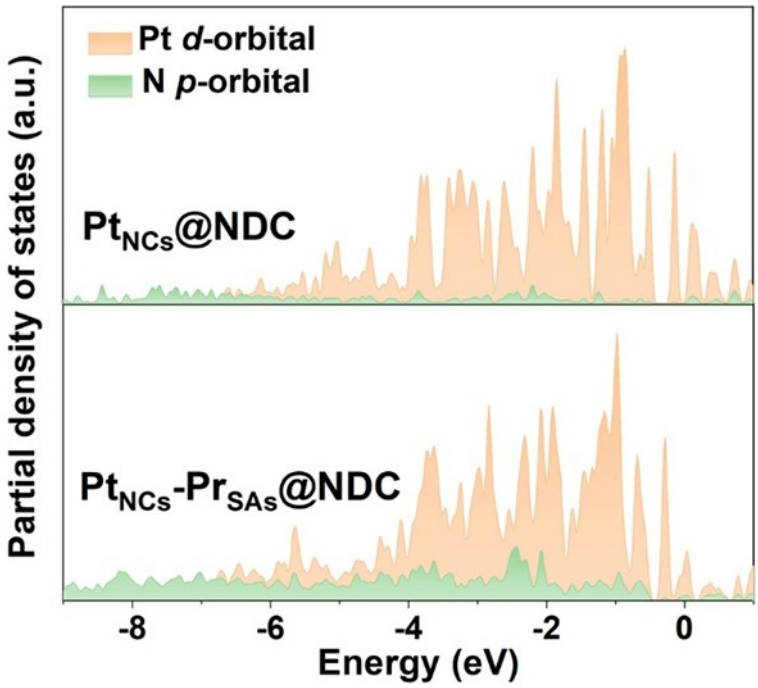

Fig. S38 The PDOS of the Pt *d*-orbital and N *p*-orbital in Pt_{NCs}@NDC and Pt_{NCs}-Pr_{SAs}@NDC.

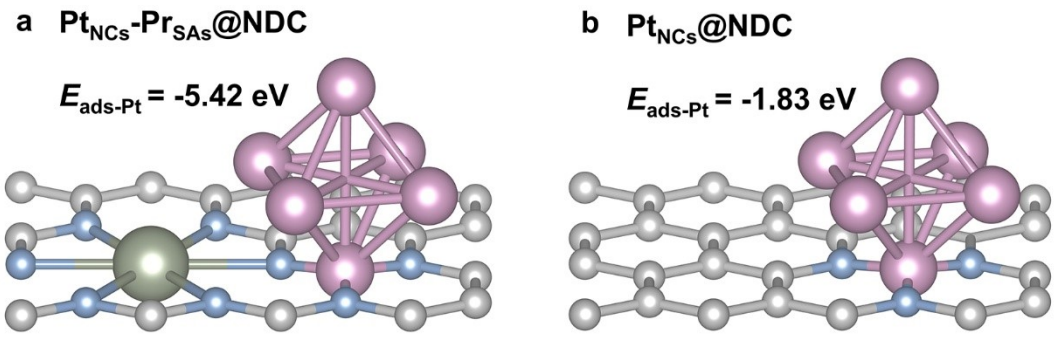

Fig. S39 Adsorption energy of Pt_{NCs} on (a) Pr_{SAs}@NDC substrate and (b) NDC substrate.

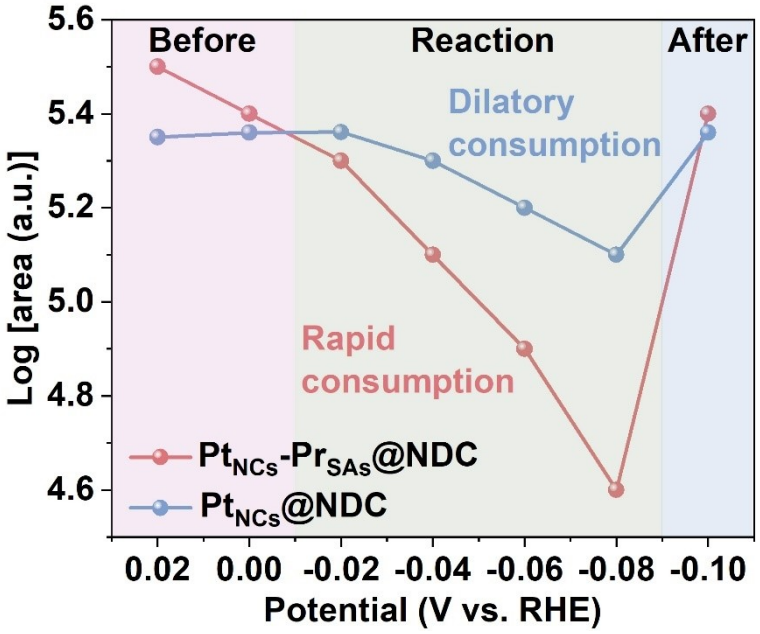

Fig. S40 Potential-depended logarithmic area of interfacial water from in situ Raman spectrum.

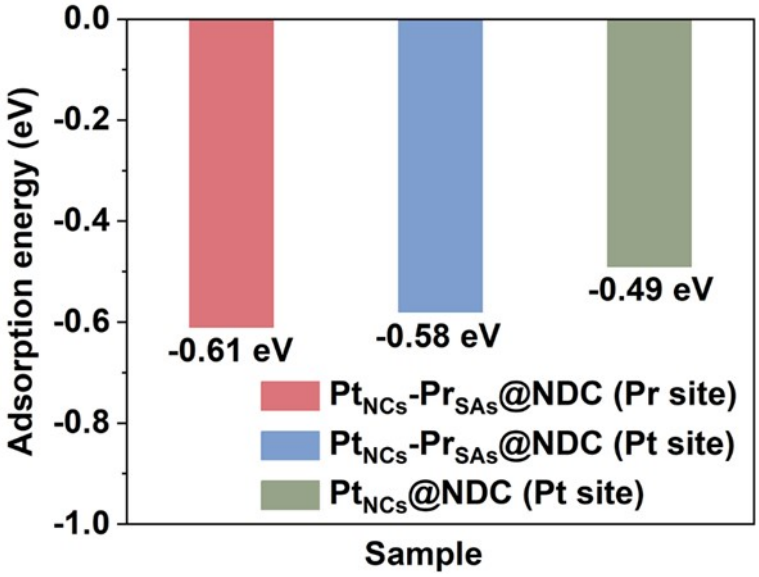

Fig. S41 H_2O adsorption energy on Pr and Pt sites in Pt_{NCs}-Pr_{SAs}@NDC, and Pt site in Pt_{NCs}@NDC.

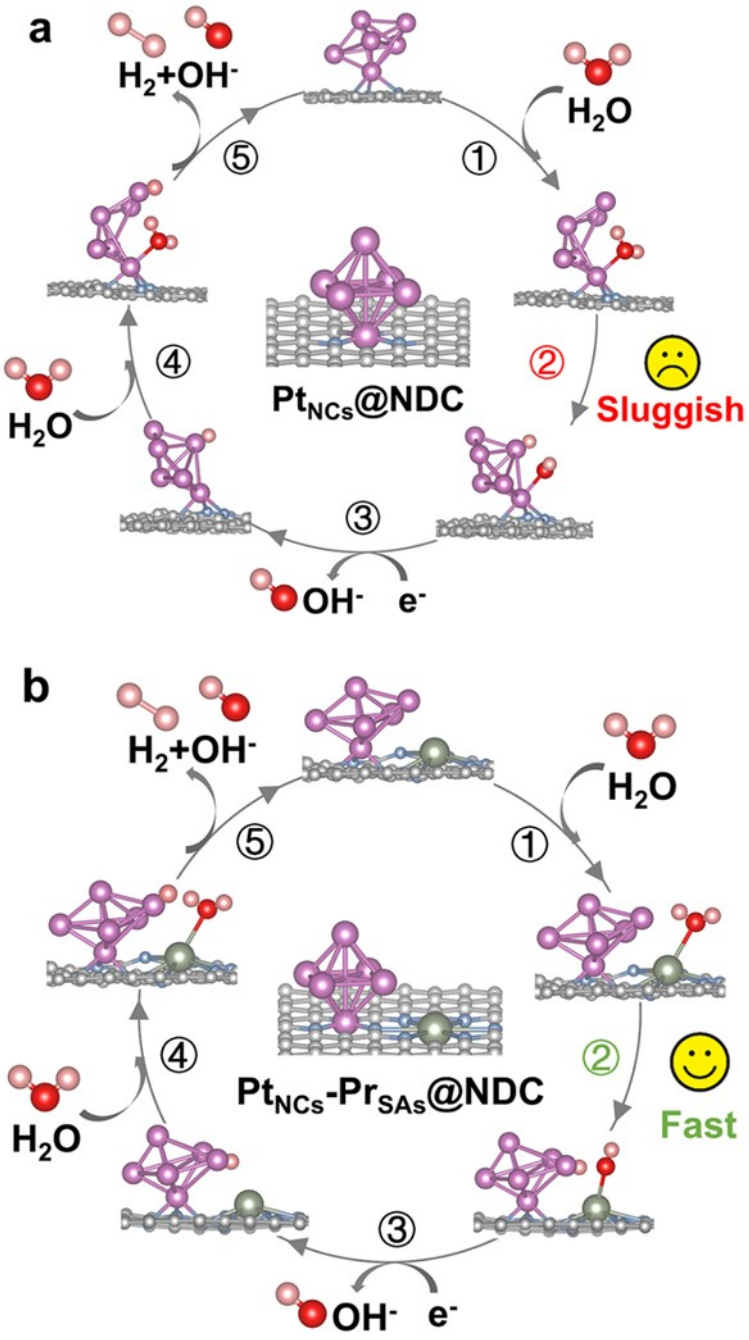

Fig. S42 Mechanism of alkaline HER of (a) Pt_{NCs}@NDC and (b) Pt_{NCs}-Pr_{SAs}@NDC.

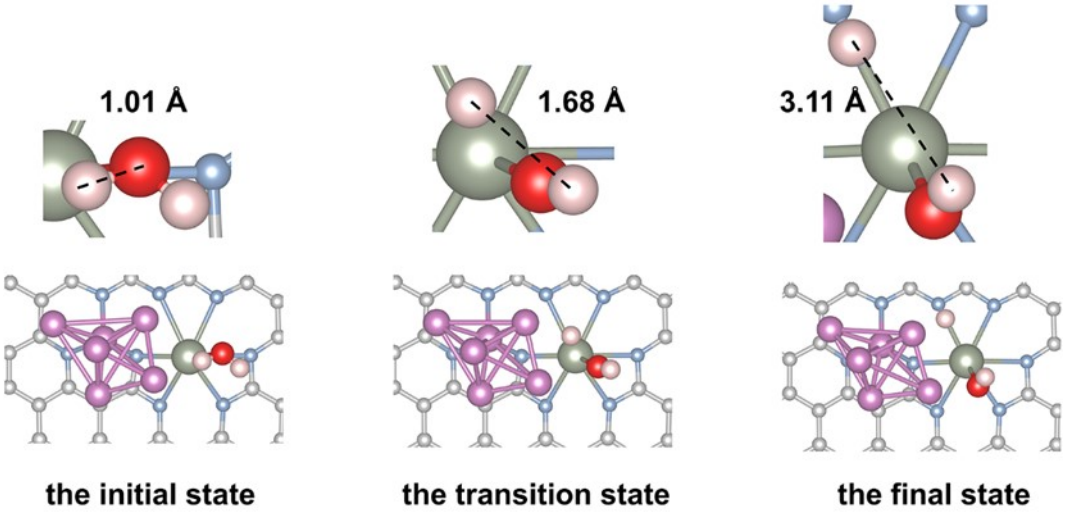

Fig. S43 The equilibrium distance of the H-OH bond in different states during the water dissociation process catalyzed by Pt_{NCs}-Pr_{SAs}@NDC.

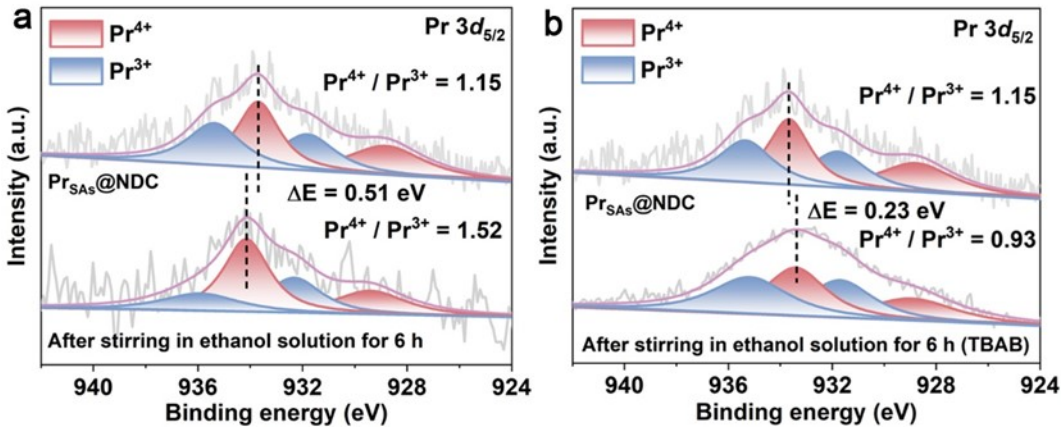

Fig. S44 Comparison of Pr 3*d* XPS spectra of the Pr_{SAs}@NDC catalyst before and after being stirred for 6 h in ethanol solution (a) without and (b) with TBAB.

Rare earth on graphite behaves like lithium and alkaline earth metals, which means they are highly water and oxygen sensitive compounds.[23,24] To further elucidate the inhibitory effect of TBAB on Pr_{SAs}@NDC oxidation, we conducted a comparison of the Pr 3*d* XPS spectra of the Pr_{SAs}@NDC catalyst before and after being stirred in an ethanol solution for 6 h. Well aligned with the reviewer's opinion, significant oxidation of Pr was observed after 6 h of stirring in the ethanol solution, as evidenced by the positive shift of the Pr $3d_{5/2}$ peak position and the increased Pr^{4+}/Pr^{3+} ratio. In contrast, when TBAB was added, the Pr $3d_{5/2}$ peak position of Pr shifted negatively, and the Pr^{4+}/Pr^{3+} ratio decreased, suggesting that TBAB can effectively suppress the oxidation of Pr in an ethanol solution.

Supplementary Tables

Table S1. The ICP results of the Pt_{NCs}-Pr_{SAs}@NDC, Pt_{NCs}@NDC, and Pr_{SAs}@NDC catalysts.

Catalysts	Pt (wt.%)	Pr (wt.%)
Pt_{NCs}-Pr_{SAs}@NDC	1.76	2.68
Pt_{NCs}@NDC	1.89	-
Pr_{SAs}@NDC	-	2.77

Inductively coupled plasma optical emission spectrometer (ICP-OES) analysis suggests a Pt and Pr content of 1.76 and 2.68 wt.% in Pt_{NCs}-Pr_{SAs}@NDC, respectively.

Table S2. Fitted XPS results of N 1*s* in Pt_{NCs}-Pr_{SAs}@NDC.

	Pyridinic N	Metal-N	Pyrrolic N	Graphitic N	Oxidized N
Binding energy (eV)	397.93	399.07	400.14	401.32	402.83
Peak area	18205	22047	19982	16225	12127

The fitted X-ray photoelectron spectroscopy (XPS) results of N 1*s* in Pt_{NCs}-Pr_{SAs}@NDC can be categorized into pyridinic (397.93 eV), metallic (399.07 eV), pyrrolic (400.14 eV), graphitic (401.32 eV), and oxidized (402.83 eV) N species. The presence of 24.89% metal-N (Metal = Pr + Pt) indicates the anchoring of metal atoms on NDC through N coordination.

Table S3. Fitted XPS results of Pt 4*f* in Pt_{NCs}-Pr_{SAs}@NDC and Pt_{NCs}@NDC.

Catalysts		**Fitted results of Pt 4*f***			
Pt_{NCs}-Pr_{SAs}@NDC	Valence state	Pt^0		Pt^{2+}	
	Binding energy (eV)	71.37	74.76	72.29	75.70
	Peak area	17736	23611	11841	12234
	Pt^0 / Pt^{2+}	1.72			
Pt_{NCs}@NDC	Valence state	Pt^0		Pt^{2+}	
	Binding energy (eV)	71.58	74.95	72.45	75.89
	Peak area	13184	17772	9244	10114
	Pt^0 / Pt^{2+}	1.60			

The obviously lowered binding energy of Pt 4*f* suggests an increased electron density and a decreased valence state in Pt_{NCs}-Pr_{SAs}@NDC compared with those in Pt_{NCs}@NDC.

Table S4. Fitted XPS results of Pr $3d_{5/2}$ in Pt_{NCs}-Pr_{SAs}@NDC and Pr_{SAs}@NDC.

Catalysts		**Fitted results of Pr $3d_{5/2}$**			
Pt_{NCs}-Pr_{SAs}@NDC	Valence state	Pr^{4+}		Pr^{3+}	
	Binding energy (eV)	928.93	934.04	932.57	935.53
	Peak area	2119	2604	2207	1593
	Pr^{4+} / Pr^{3+}	1.24			
Pr_{SAs}@NDC	Valence state	Pr^{4+}		Pr^{3+}	
	Binding energy (eV)	928.80	933.68	931.81	935.36
	Peak area	2637	3397	2468	2775
	Pr^{4+} / Pr^{3+}	1.15			

The notable positive shift of Pr $3d$ in Pt_{NCs}-Pr_{SAs}@NDC compared with that in Pr_{SAs}@NDC implies the Pr→Pt electron transfer, which effectively alleviates the local charge imbalance and leads to improved covalency of Pt-N bond.

Table S5. EXAFS fitting parameters at the Pt and Pr L_3-edge in various samples (S_0^2 = 0.85). C.N.: coordination number; R: bond length; σ^2: Debye-Waller factors; ΔE: the inner potential correction. R factor: goodness of fit. * Fitting with fixed parameter.

Sample	Path	C.N.	R (Å)	$\sigma^2\times10^3$ ($Å^2$)	ΔE (eV)	R factor
Pt foil	Pt-Pt	12*	2.76±0.01	4.7±0.2	8.4±0.4	0.001
PtO_2	Pt-O	5.7±1.3	1.99±0.01	2.4±2.3	9.6±2.7	0.017
Pt_{NCs}-Pr_{SAs}@NDC	Pt-N	2.1±0.5	2.03±0.02	4.7±2.3	9.9±3.2	0.011
	Pt-Pt	5.7±1.1	2.76±0.01	7.7±1.2	9.6±2.0	
Pt_{NCs}@NDC	Pt-N	2.4±0.7	2.06±0.02	7.5±3.4	10.5±3.2	0.019
	Pt-Pt	4.6±1.5	2.75±0.02	7.4±2.1	8.7±3.0	
Pr_6O_{11}	Pr-O	5.7±1.4	2.34±0.02	18.8±6.5	4.6±1.4	0.011
Pt_{NCs}-Pr_{SAs}@NDC	Pr-N	5.0±1.3	2.54±0.02	13.6±4.9	3.5±1.7	0.013
Pr_{SAs}@NDC	Pr-N	6.0±1.5	2.51±0.04	29.9±11.1	0.7±2.6	0.018

The greatly shortened Pt-N bond length in Pt_{NCs}-Pr_{SAs}@NDC (2.03 Å) compared with that in Pt_{NCs}@NDC (2.06 Å), ensures highly improved the Pt-N covalency and thus the stability of Pt_{NCs}.

Table S6. Comparison of catalytic performance of the Pt_{NCs}-Pr_{SAs}@NDC catalyst in this work and the representative noble metal-based catalysts reported in the literatures.

Catalysts	Noble metal	Loading (wt.%)	Overpotential at 10 mA·cm^{-2} (mV)	Tafel (mV·dec^{-1})	Mass activity (A·mg$_{noble\ metal}^{-1}$)	References
Pt_{NCs}-Pr_{SAs}@NDC	Pt	1.76	7	31.3	25.4 A mg_{Pt}^{-1}@100 mV	This work
Pt SACs-$NiCrO_3$/NF	Pt	1.45	23	38.73	0.382 A mg_{Pt}^{-1}@100 mV	*Adv. Funct. Mater.*, 2024, **35**, 2416678.
Pt/CoFe/NF	Pt	1.2	16	31.4	0.547A mg_{Pt}^{-1}@100 mV	*ACS Catal.*, 2024, **14**, 14937-14946.
PtSA-X-CeO_{2-x}/rGO	Pt	0.8	33	57.9	15.46 A mg_{Pt}^{-1}@50 mV	*Angew. Chem. Int. Ed.*, 2024, **63**, e202406650.
Pt1/$Ni(OH)_2$/C	Pt	1.57	55	52.1	0.82 A mg_{Pt}^{-1}@90 mV	*Energy Environ. Sci.*, 2023, **16**, 1035-1048.
LD-PtWNPs	Pt	37.6	59	52	1 A mg_{Pt}^{-1}@17.5 mV	*Nano Res.*, 2024, **17**, 3819-3826.
Ru SAs/WCx	Ru	1.26	21	50.1	17.2 A mg_{Ru}^{-1}@100 mV	*J. Am. Chem. Soc.*, 2024, **146**, 4883.
Pt-NiO/Gr-SUS	Pt	0.09	79	41	25 A mg_{Pt}^{-1}@100 mV	*ACS Nano*, 2022, **16**, 930-938.
Pt/Co_3O_4	Pt	0.63	21	33	3.38 A mg^{-1}@50 mV	*Nano Lett.*, 2024, **24**, 11286.

Compared with most of the reported noble metal-based electrocatalysts, the Pt_{NCs}-Pr_{SAs}@NDC electrocatalyst is superior in these aspects and achieves ultrahigh mass activity (25.4 A mg_{Pt}^{-1} at an overpotential of 100 mV), which is 25.4 times of that of commercial Pt/C (1.0 A mg_{Pt}^{-1} at an overpotential of 100 mV).

Table S7. EIS results of samples by fitting with the proposed equivalent circuit.

	Pt_{NCs}-Pr_{SAs}@NDC	Pt_{NCs}@NDC
R_s (Ω)	2.8	2.3
R_{ct} (Ω)	11.2	47.7

The lower charge transfer resistance (R_{ct}) in Pt_{NCs}-Pr_{SAs}@NDC compared with that in Pt_{NCs}@NDC implies enhanced charge transfer.

Table S8. Comparison of the turnover frequency (TOF) in 1.0 M KOH electrolyte.

Catalyst	Overpotential (mV)	TOF ($H_2 \cdot s^{-1}$)	Reference
Pt_{NCs}-Pr_{SAs}@NDC	100	25.7	This work
RuNP@RuNx-OFC/NC	10	0.49	*Appl. Catal. B: Environ.,* 2022, **307**, 121193.
Pt@DG	10	6.74	*J. Am. Chem. Soc.,* 2022, **144**, 2171-2178.
Pt/C_{60}-2	10	5.55	*Nat. Commun.,* 2023, **14**, 2460.
RuNP-RuSA@CFN	50	3.2	*Adv. Funct. Mater.,* 2023, **33**, 2213058.
Cu-Ru/$RuSe_2$ NS	100	0.88	*Adv. Mater.,* 2023, **35**, 2300980.
RuFe/FeNC	25	0.21	*Energy Environ. Sci*., 2025,**18**, 1984-1991.
Eu_2O_3-NiC	150	1.59	*Adv. Funct. Mater.,* 2024, **34**, 2409324.
RuNi/N	100	1.7	*Nat. Commun*., 2024, **15**, 7179.
AC-Ir NSs	30	3.6	*Nat. Commun.,* 2022, **13**, 4200.
W-ACs	50	0.12	*Nat. Commun*., 2022, **13**, 763.
PtW/M-NC	100	5.5	*ACS Nano,* 2024, **18**, 33696.
(c/o)-$CoSe_2$-W	80	1.9	*Adv. Mater.,* 2024, **36**, 2401880.
c-RP DWNT/C	50	0.48	*Adv. Energy Mater.,* 2024, **14**, 2304269.

Here, the Pt_{NCs}-Pr_{SAs}@NDC delivers a much larger TOF value of 25.7 $H_2 \cdot s^{-1}$ than that of commercial Pt/C (1.1 $H_2 \cdot s^{-1}$) and other reported noble metal-based electrocatalysts, indicating a high H_2 production efficiency for Pt_{NCs}-Pr_{SAs}@NDC.

Table S9. Comparison of catalytic performance among representative rare earth-Pt catalysts and single-atom-nanocluster catalysts reported in the literatures.

Catalysts	Overpotential at 10 mA·cm^{-2} (mV)	Tafel (mV·dec^{-1})	Mass activity (A·mg$_{noble\ metal}^{-1}$)	Stability test (h@mA cm^{-2}/CVs)	References
Pt_{NCs}-Pr_{SAs}@NDC	7	31.3	25.4 A mg_{Pt}^{-1}@100 mV	200@1000 10000 CVs	This work
JH-Pt_2Tb/C	17	46	12A mg_{Pt}^{-1}@50 mV	100@1000	*Adv. Mater*., 2025, **37**, 2506936.
PtRu/ CNT@CeO_{2-x}	75@100 mA·cm^{-2}	48	12.3 mA μg_{Pt+Ru}^{-1}	24@50	*J. Am. Chem. Soc.,* 2024, **146**, 21453-21465.
PtSA-X-CeO_{2-x}/rGO	33	57.9	15.46 A mg_{Pt}^{-1}@50 mV	44@10	*Angew. Chem. Int. Ed.,* 2024, **63**, e202406650.
CeO_2 NW@PtCu	7	20.3	2.9 A mg_{Pt}^{-1}@100 mV	2000 CVs	*Nano energy,* 2025, **142**, 111254.
ALD Pt/NGN	47	52	2 A mg_{Pt}^{-1}@50 mV	1000 CVs	*Nano Res.,* 2024, **17**, 3819-3826.
Pt-AC/Cr-N-C	19	30	7.9 A mg_{Pt}^{-1}@50 mV	24@10	*J. Am. Chem. Soc.,* 2023, **145**, 21432.
Pt_n-S/Ni_1-NC	19	41	5.99 A mg_{Pt}^{-1}@100 mV	105@10	*Adv. Mater*., 2025, e16082.
RuSA/NP-PNCFs	8	21.7	1.07 A mg_{Ru}^{-1}@25 mV	600@1000	*Joule,* 2024, **8**, 1-14.
Ru/Ni-N_4C-300	15	43.2	3.2 A mg_{Ru}^{-1}@100 mV	20@10	*Adv. Funct. Mater*., 2024, **35**, 2416071.
Pt_{1+n}/Ni_3S_2	17	14.6	0.48 A mg_{Pt}^{-1}@100 mV	110@200	*Appl. Catal. B: Environ. Energy,* 2024, **354,** 124074.

When compared with RE-doped Pt-based catalysts, even though both endeavors aim to leverage RE elements for the regulation of the electronic structure of Pt to facilitate an efficient HER, majority of the reported research introduces RE via alloying or surface adsorption, which may result in the entrapment or non-uniform distribution of RE atoms. We innovatively put forward an architecture of RE single atoms and Pt nanoclusters synergizing through a N bridge so that RE single atoms are atomically dispersed and strongly coupled with Pt nanoclusters through chemical bonds, thereby achieving more precise and efficient long-range electronic modulation.

Although the concept of single-atom-cluster synergy has been put forward, prior research has predominantly concentrated on the synergy between transition metal single atoms and Pt or Ru clusters. In this study, RE single atoms featuring unique 4*f* electronic structures are incorporated, which not only strengthens the Pt-N bond but also, due to their strong Lewis acid

characteristics, prevents the Pt sites from being occupied by OH_{ads} and facilitates water dissociation, thereby exhibits excellent performance in both activity and high-current-density stability.

Table S10. The HER performance of Ce-, Sm-, and Gd-based Pt_{NCs}-RE_{SAs}@NDC catalysts.

Catalysts	Overpotential at 10 mA·cm^{-2} (mV)	Stability (h/mA·cm^{-2})
Pt_{NCs}-Ce_{SAs}@NDC	12	100/10
Pt_{NCs}-Sm_{SAs}@NDC	10	100/10
Pt_{NCs}-Gd_{SAs}@NDC	9	100/10

This catalyst designing principle is also extendable to other light RE_{SAs} such as Ce_{SAs}, Sm_{SAs}, and Gd_{SAs}, introduction of which leads to a significant boost in both the activity and stability of Pt_{NCs}, i.e., Pt_{NCs}-Ce_{SAs}@NDC: η_{10} = 12 mV, 100 h@10 mA·cm^{-2}, Pt_{NCs}-Sm_{SAs}@NDC: η_{10} = 10 mV, 100 h@10 mA·cm^{-2}, and Pt_{NCs}-Gd_{SAs}@NDC: η_{10} = 9 mV, 100 h@10 mA·cm^{-2}.

Table S11. Comparison of HER activity of Pt_{NCs}-Pr_{SAs}@NDC with other reported representative noble metal-based HER catalysts using 1.0 M KOH as electrolyte.

Catalysts	Overpotential at 10 mA·cm^{-2} (mV)	Overpotential at 500 mA·cm^{-2} (mV)	Overpotential at 1000 mA·cm^{-2} (mV)	Stability (h/mA·cm^{-2})	References
Pt_{NCs}-Pr_{SAs}@NDC	7	94	150	200/1000	This work
Ru-2.3	9	145	169	100/1000	*Nat. Commun.*, 2022, **13**, 3958.
Ru@Cu-TiO_2/Cu	16	112	-	250/200	*J. Am. Chem. Soc.*, 2023, **145**, 21419-21431.
Pt–Ni@NiMoN	11	90	-	45/500	*Energy Environ. Sci.*, 2023,**16**, 4584-4592.
MoO_2@Ru NT	22	89	131	100/1000	*Adv. Energy Mater.*, 2023, **13**, 2301492.
RuCo@Ru SA Co SA-NMC	5	195	255	400/50	*Adv. Funct. Mater.,* 2023, **33**, 2301804.
PtSA/NDPCM	20	271	465	100/10	*Adv. Funct. Mater.*, 2023, **33**, 2304852.

The Pt_{NCs}-Pr_{SAs}@NDC electrocatalysts employing rare earth single atoms (RE_{SAs}) can reach industrial current densities of 500 and 1000 mA·cm^{-2} at overpotentials of 94 and 150 mV, respectively, which are higher than most of those noble metal-based electrocatalysts.

Table S12. ICP results of the Pt_{NCs}-Pr_{SAs}@NDC catalyst before and after the high current density stability test.

Samples	Pt (wt.%)	Pr (wt.%)
Initial	1.76	2.68
After the high current density stability test	1.73	2.63

The dissolution rate of Pt atoms in Pt_{NCs}-Pr_{SAs}@NDC as determined by the ICP-OES is only 1.7% after such stability test.

The Molar dissolution rate of Pt

The durability test was running for 200 h at 1000 mA·cm^{-2}. The tests were performed using a three-electrode setup in an electrolytic cell containing 100 mL of N_2-saturated 1.0 M KOH solution. The Pt content in the electrolyte after the durability test was also determined by ICP-OES. We defined the molar number of Pt in the catalyst before the durability test as the initial amount of Pt, the molar number of Pt in the electrolyte after the durability test as the amount of Pt dissolved, and the ratio of the amount of Pt dissolved to the initial amount of Pt as the molar dissolution rate of Pt.[25]

The molar of dissolved Pt is 0.03 wt.%, the molar of initial Pt in electrode is 1.76 wt.%, therefore the dissolution of Pt during long term water electrolysis can be calculated based on the formula above, i.e., the molar dissolution rate of Pt atoms is 1.7%.

$$The\ molar\ dissolution\ rate\ of\ Pt\ (\%) = \frac{The\ molar\ of\ dissolved\ Pt}{The\ molar\ of\ intial\ Pt\ in\ electrode}$$

$$= 0.03/1.76 \times 100\% = 1.7\% \qquad (6)$$

Table S13. Comparison of the AEMWE activity and stability with those previously reported Pt-based catalysts.

Samples (Pt loading)	Anodic catalysts	Activity ($V/mA \cdot cm^{-2}$)	Stability ($h/mA \cdot cm^{-2}$)	References
Pt_{NCs}-Pr_{SAs}@NDC ($0.044\ mg_{Pt} \cdot cm^{-2}$)	NiFe LDH	1.75/1000	500/500	This work
Pt nanoparticles ($1.6\ mg_{Pt} \cdot cm^{-2}$)	IrO_2	1.69/1000	150/800	*ECS Trans*., 2016, **75**, 1143-1146.
Pt-NiO_x-H ($0.050\ mg_{Pt} \cdot cm^{-2}$)	NiFe LDH	1.74/1000	120/500	*Angew. Chem. Int. Ed.,* 2025, e202422062.
Pt-AC/Cr-N-C ($0.050\ mg_{Pt} \cdot cm^{-2}$)	NiFe LDH	1.8/500	100/500	*J. Am. Chem. Soc.,* 2023, **145**, 21432-21441.
PtNiNb ($0.05\ mg_{Pt} \cdot cm^{-2}$)	PtIr	1.98/1000	500/1000	*Nat. Commun*., 2023, **14**, 5389.
Pt/C ($1\ mg_{Pt} \cdot cm^{-2}$)	AEI	1.73/1000	12/1000	*Chem. Eng. J.,* 2023, **467**, 143442.
$Pt(OH)(O_3)$/Co(P) ($0.029\ mg_{Pt}\ cm^{-2}$)	Ir/C	1.8/1000	100/400	*Nat Commun*., 2022, **13**, 3822.
Pt/C ($1\ mg_{Pt} \cdot cm^{-2}$)	FCNal	1.73/1000	36/1000	*Chem. Eng. J.,* 2025, **504**, 158217.
SL-Pt cluster ($0.5\ mg_{Pt} \cdot cm^{-2}$)	IrO_2	1.74/1000	48/1000	*Adv. Funct. Mater.,* 2023, **33**, 2212752.
Pt SACs-$NiCrO_3$/NF ($0.21\ mg_{Pt} \cdot cm^{-2}$)	NiFeOxHy	1.5/100	100/100	*Adv. Funct. Mater*., 2024, **35**, 2416678.

The AEMWE using Pt_{NCs}-Pr_{SAs}@NDC (with only $0.044\ mg_{Pt} \cdot cm^{-2}$ loading) as the cathode catalyst exhibits an ultralow potential ($1.75\ V@1000\ mA \cdot cm^{-2}$) and high stability ($500\ h@500\ mA \cdot cm^{-2}$), indicating its great potential for industrial-scale water electrolysis.

Table S14. Standard deviations (Å) of positions of the atoms in Pt_{NCs}@NDC and Pt_{NCs}-Pr_{SAs}@NDC at 300 and 353 K, respectively.

Samples	Temperature (K)	Total (Å)	NDC (Å)	Pt (Å)	Pr (Å)
Pt_{NCs}-Pr_{SAs}@NDC	300	0.24	0.24	0.21	0.16
Pt_{NCs}@NDC		0.44	0.45	0.35	-
Pt_{NCs}-Pr_{SAs}@NDC	353	0.28	0.28	0.22	0.16
Pt_{NCs}@NDC		0.36	0.36	0.50	-

The *ab* initio MD simulations at 300 and 353 K show a much smaller standard deviation difference for Pt in Pt_{NCs}-Pr_{SAs}@NDC (0.20 to 0.21 Å) than in Pt_{NCs}@NDC (0.35 to 0.50 Å), meaning that the enhanced Pt-N bond covalency can effectively suppress thermal vibrations of Pt_{NCs}, i.e., good stability for AEMWE.

References

1. K. Li, S. Lin, Y. Li, Q. Zhuang and J. Gu, *Angew. Chem. Int. Ed*., 2018, **57**, 3439.
2. J. Gao, Y. Hu, Y. Wang, X. Lin, K. Hu, X. Lin, G. Xie, X. Liu, K. M. Reddy, Q. Yuan and H. J. Qiu, *Small*, 2021, **17**, 2104684.
3. X. Wang, L. Zhao, X. Li, Y. Liu, Y. Wang, Q. Yao, J. Xie, Q. Xue, Z. Yan, X. Yuan and W. Xing, *Nat. Commun*., 2022, **13**, 1596.
4. X. Yuan, L. Chng, J. Yang and J. Ying, *Adv. Mater*., 2020, **32**, 1906063.
5. L. Wang, M. Ma, C. Zhang, H. Chang, Y. Zhang, L. Li, H. Chen and S. Peng, *Angew. Chem. Int. Ed*., 2024, **63**, e202317220.
6. G. Sun, Y. Xu, Y. Xia, D. Kong, J. Zhu, D. Li, X. Liu, J. Lai, J. Chi and L. Wang, *Adv. Funct. Mater*., 2025, e12343.
7. L. Zeng, Z. Zhao, Q. Huang, C. Zhou, W. Chen, K. Wang, M. Li, F. Lin, H. Luo, Y. Gu, L. Li, S. Zhang, F. Lv, G. Lu, M. Luo and S. Guo, *J. Am. Chem. Soc*., 2023, **145**, 21432-21441.
8. Y. Liu, H. Hu, K. Wang, J. Huang and D. Wang, *Adv. Energy Mater*., 2025, e04101.
9. Y. Du, Y. Luo, K. Shi, P. Zuo, Q. Zhang, Z. Zheng, B. Sun and J. Xie, *Adv. Mater*., 2025, **37**, 2502095.
10. G. Kresse and J. Furthmüller, *Phys. Rev. B*, 1996, **54**, 11169-11186.
11. J. Perdew, K. Burke and M. Ernzerhof, *Phys. Rev. Lett*.,1996, **77**, 3865-3868.
12. P. Blöchl, *Phy. Rev. B*, 1994, **50**, 17953-17979.
13. S. Grimme, J. Antony, S. Ehrlich and H. Krieg, *J. Chem. Phys*., 2010, **132**, 154104.
14. R. Tesch and P. Kowalski, *Phys. Rev. B*, 2022, **105**, 195153.
15. K. Benyelloul, H. Aourag and B. Bouhafs, *Int. J. Hydrogen Energ*., 2016, **41**, 11254-11263.
16. V. Deringer, A. Tchougréeff and R. Dronskowski, *J. Phys. Chem. A*, 2011, **115**, 5461-5466.

17. S. Maintz, V. Deringer, A. Tchougréeff and R. Dronskowski, *J. Comput. Chem*., 2016, **37**, 1030-1035.
18. D. Bylander and L. Kleinman, *Phys. Rev. B*, 1992, **46**, 13756-13761.
19. S. Nosé, *J. Chem. Phys*., 1984, **81**, 511-519.
20. J. He, W. Fang and R. Long, *J. Mater. Chem. A*, 2020, **8**, 607.
21. J. He, W. Fang and R. Long, *J. Phys. Chem. Lett*., 2018, **9**, 4834-4840.
22. G. Henkelman, B. Uberuaga and H. Jónsson, *J. Chem. Phys*., 2000, **113**, 9901-9904.
23. M. Makrini, D. Guérard, P. Lagrange and A. Hérold, *Physica B+C*, 1980, **99**, 481-485.
24. W. E. Craven and W. Ostertag, *Carbon*, 1966, **4**, 223-226.
25. C. Hu, G. Xing, W. Han, Y. Hao, C. Zhang, Y. Zhang, C. Kuo, H. Chen, F. Hu, L. Li and S. Peng, *Adv. Mater*., 2024, **36**, 2405763.